

# A self-breathing electrode enabled by interface regulation and gradient wettability engineering for industrial H<sub>2</sub>O<sub>2</sub> electrosynthesis

Received: 10 July 2025

Accepted: 7 January 2026

Published online: 15 January 2026

 Check for updatesYe Tian<sup>1</sup>, Luwei Pei<sup>1,2</sup>, Shuo Wang<sup>1,2</sup>, Kongrui Yu<sup>1</sup>, Yuqing Xu<sup>1</sup>, Xiaoqin Ye<sup>2</sup>, Songming Zhu<sup>1,3</sup>, Ying Liu<sup>1,3</sup>, Zhenghua Zhang<sup>4</sup>✉ & Zhangying Ye<sup>1,3</sup>✉

High-performance gas diffusion electrodes (GDEs) are essential for electrochemical H<sub>2</sub>O<sub>2</sub> production, yet conventional catalyst layers (CLs) suffer from PTFE-fused encapsulation and disordered pores that create mass-transport bottlenecks and suppress three-phase interface (TPI) formation. Here, we introduce a non-fused particulate-packed catalyst/binder interface and elucidate the mechanisms governing TPI formation through 3D reconstruction and mesoscale LBM analyses. Guided by these insights, we construct a hierarchical gradient CL with ordered porosity and tunable wettability contrast, and multiscale simulations together with in-situ breakthrough and microfluidic experiments confirm capillarity-driven electrolyte displacement and directional self-transport of H<sub>2</sub>O<sub>2</sub>, enabling stable Faradaic efficiencies >85% at 300 mA cm<sup>-2</sup> for 300 h. We further develop a 400 cm<sup>2</sup> four-unit self-breathing flow-through stack integrating thermal, fluidic, and electronic systems for continuous, oxygen-free, low-cost H<sub>2</sub>O<sub>2</sub> generation. This work offers a fundamental design framework for advanced GDEs and demonstrates a milestone integrated self-breathing H<sub>2</sub>O<sub>2</sub> electrosynthesis system with commercial viability.

Hydrogen peroxide (H<sub>2</sub>O<sub>2</sub>) is a green oxidant widely used in sustainable chemical synthesis and pollutant treatment, serving as a cornerstone of modern green chemistry<sup>1,2</sup>. Currently, over 95% of H<sub>2</sub>O<sub>2</sub> is produced via the anthraquinone process—a complex route that generates substantial hazardous by-products with high energy consumption and cost<sup>3</sup>. As a sustainable alternative, the electrochemical two-electron oxygen reduction reaction (2e<sup>-</sup> ORR) enables economical, on-site H<sub>2</sub>O<sub>2</sub> production using only air, water, and renewable electricity. This decentralized approach supports the chemical industry's green transition and aligns with carbon neutrality goals<sup>4–6</sup>.

Gas diffusion electrodes (GDEs) represent the most promising electrode architecture for 2e<sup>-</sup> ORR, as they physically separate gas and liquid phases and help overcome oxygen solubility limitation<sup>7</sup>. Despite decades of catalyst-focused research, GDEs continue to suffer from well-known “flooding” under high current densities—a key bottleneck to industrial deployment<sup>8–10</sup>. Strategies such as increasing polytetrafluoroethylene (PTFE) content or incorporating electrospun hydrophobic layers can mitigate flooding but often compromise conductivity due to a trade-off between hydrophobicity and electron transport<sup>11–13</sup>. Even recent strategies like crack engineering that

<sup>1</sup>College of Biosystems Engineering and Food Science, Zhejiang University, Hangzhou, China. <sup>2</sup>Zhejiang Epai Technology Co. Ltd, Hangzhou, China. <sup>3</sup>Key Laboratory of Equipment and Informatization in Environment Controlled Agriculture, Ministry of Agriculture and Rural Affairs, Hangzhou, China. <sup>4</sup>Membrane & Nanotechnology-Enabled Water Treatment Center, Tsinghua Shenzhen International Graduate School, Tsinghua University, Shenzhen, China.

✉ e-mail: [zhenghua.zhang@sz.tsinghua.edu.cn](mailto:zhenghua.zhang@sz.tsinghua.edu.cn); [yzyzju@zju.edu.cn](mailto:yzyzju@zju.edu.cn)

facilitate gas access fail to fully prevent flooding in catalyst regions beyond the cracks<sup>14</sup>. These results expose a critical paradox: while catalyst innovation has flourished, GDE structural limitations continue to impede industrial adoption. This persistent challenge highlights a critical knowledge gap in electrode engineering—the lack of established design principles for three-phase interface (TPI) construction has confined structural optimization to empirical trial-and-error approaches.

Traditionally, catalyst layers (CLs) are fabricated by depositing a slurry of catalyst particles, PTFE, and alcohol-based solvents onto a gas diffusion layer (GDL)<sup>12,15</sup>. To ensure the hydrophobicity of the PTFE, calcination is typically required to remove residual surfactants<sup>11,16</sup>. However, this fabrication route conceals three critical limitations. (1) Slurry dispersion issue. PTFE tends to aggregate and separate from catalysts in alcohol media, especially at high loadings<sup>17,18</sup>. (2) Covered and segregated interface structure. Upon calcination, PTFE melts non-uniformly: some coats catalyst surfaces, forming an insulating armor that increases resistance, while the rest forms isolated hydrophobic islands detached from the catalyst<sup>12,16,19,20</sup>. This dual structure imposes a PTFE content threshold—representing the root of the long-standing trade-off between hydrophobicity and electron transport in GDEs. (3) The emergence of spatial disorder: the coexistence of coated and segregated PTFE domains results in randomly distributed wettability and pore structures, creating a mass transport maze that disrupts capillary-driven convection and obstructs removal of in situ generated H<sub>2</sub>O<sub>2</sub>. These findings highlight that ambiguous catalyst-binder interfaces and disordered CL structures fundamentally limit GDE performance. Rather than incremental improvements within this constrained paradigm, transformative advances require a complete architectural redesign of the CL.

Bridging this gap in interface engineering demands a systematic understanding of the pore architecture arising from catalyst–binder interactions and its role in TPI formation within the CL<sup>21</sup>. However, conventional tools—scanning electron microscopy (SEM), contact angle (CA) measurements, and N<sub>2</sub> adsorption/desorption—fail to resolve true 3D microstructures. SEM provides only 2D projections; CA is affected by surface roughness and binder exposure<sup>6,22</sup>; and N<sub>2</sub> adsorption/desorption offers only statistical pore data, lacking spatial context. To date, the actual spatial arrangement of catalyst/binder components and their resulting pore structures in CLs remain poorly understood. Equally unclear is how the triple-phase microenvironment controls 2e<sup>-</sup> ORR mass transport, creates active zones, and accelerates reaction kinetics.

Here, a non-fused particulate-packed catalyst/binder interface (Fig. 1) is introduced, in which discrete PTFE is embedded within the catalyst matrix to form a packed-contact, pore-percolated structure that exposes active sites and supports dense TPIs. Using focused ion beam-scanning electron microscopy (FIB-SEM) 3D reconstruction, the Lattice Boltzmann Method (LBM), and the Quartet Structure Generation Set (QSGS), electrolyte intrusion was quantitatively revealed to be governed by the coupling of wettability and pore geometry, uncovering the structural origin of TPI formation. Guided by these findings, an ordered CL with controlled wettability gradients and hierarchical pores was subsequently developed, and multiscale simulations together with microfluidic experiments validated that Laplace pressure-driven directional H<sub>2</sub>O<sub>2</sub> transport occurs through the CL. The optimized electrodes were operated stably for over 500, 300, and 50 h at 15, 300, and 400 mA cm<sup>-2</sup>, respectively, maintaining FE above 80%. Finally, we scaled up the design to a 400 cm<sup>2</sup> five-cell modular flow-through cell stack, integrating electronic, thermal, and fluidic subsystems into a commercially viable in situ H<sub>2</sub>O<sub>2</sub> synthesis platform. This fully assembled platform enables in situ H<sub>2</sub>O<sub>2</sub> production using only air, water, and electricity, achieving a cost as low as \$0.381 kg<sup>-1</sup>—marking a key step toward decentralized, cost-effective and low-carbon manufacturing of H<sub>2</sub>O<sub>2</sub>.

## Results

### Non-fused particulate-packed interface structure

To investigate the effect of the catalyst/binder interface structure on electrochemical H<sub>2</sub>O<sub>2</sub> production, two GDEs were fabricated using PTFE as the binder: one with a conventional fused–segregated interface (FSE), and another with a non-fused particulate-packed interface (PPE), prepared via different deposition methods (Supplementary Fig. 1; Methods). In the FSE electrode, a significant portion of CB is covered by fused PTFE, while in localized regions, PTFE coalesces into large patches (Fig. 2a), forming hydrophobic islands—a phenomenon previously reported<sup>6,12,22</sup>. In contrast, PPE exhibits discrete PTFE particles co-packed with CB in a stacked arrangement (Fig. 2a). To isolate the effect of microscale interface structure, key deposition variables were controlled to yield comparable CL thicknesses—a factor known to influence performance<sup>23</sup>. Cross-sectional SEM (Fig. 2b) shows only a minor difference in thickness between FSE (110.2 μm) and PPE (119.8 μm), likely due to hot-press-induced densification. PTFE content was also adjusted to match initial wettability (CA = 150°, Fig. 2c), and both used identical hydrophobic carbon paper as the gas diffusion layer (Supplementary Fig. 2). These controls ensured that microscale interface architecture was the sole performance variable. Electrolysis was conducted in a divided, self-breathing cell open to ambient air (Supplementary Fig. 3). At 15 mA cm<sup>-2</sup>, both electrodes showed similar FE (80–90%) (Fig. 2d), consistent with prior work<sup>13,24,25</sup>. However, at 300 mA cm<sup>-2</sup>, FSE dropped below 1% FE within 5 h, while PPE maintained >80% (Fig. 2e). These findings clearly demonstrate that, while both electrodes share similar macroscopic characteristics, the microscopic interface structure introduces a profound performance gulf.

To elucidate the performance disparity between the two GDEs, their physicochemical properties and O<sub>2</sub>/electrolyte mass transport behavior were systematically investigated. In the diffusion-limited open-air system used here, efficient O<sub>2</sub> delivery to active sites is essential for sustaining the 2e<sup>-</sup> ORR. Stepwise chronoamperometry (25 mA cm<sup>-2</sup> per step) was employed to monitor FE and steady-state potential under increasing current, thereby quantifying oxygen transport limitations. As shown in Fig. 2f, PPE exhibited stable potential shifts within 300 mV and consistent FE, suggesting that the reaction remained under kinetic and ohmic control without significant mass transport limitations. In contrast, FSE exhibited rising overpotentials and declining FE, signaling concentration polarization and the onset of parasitic 4e<sup>-</sup> ORR or hydrogen evolution reaction (HER). Interestingly, post-electrolysis CA was higher for FSE than PPE (Fig. 2c)—contrary to the expectation that higher hydrophobicity promotes gas diffusion. Given their identical catalyst, initial wettability, and macroscale structure, this counterintuitive result highlights a key insight: the observed difference in oxygen transport capability likely arises from variations in microscopic interface architecture. Multiscale SEM imaging revealed that PPE features a discrete particulate network, with PTFE embedded between CB domains to form a porous structure (Supplementary Fig. 4a–c), while FSE exhibits melted PTFE coverage and isolated hydrophobic domains (Supplementary Fig. 4d–f). This fused-driven restructuring significantly reduced microporosity and yielded a denser catalyst layer (Supplementary Fig. 4d). Mercury intrusion porosimetry quantitatively confirmed these structural differences, revealing that PPE exhibited higher macro-/mesopore content, greater pore volume, and lower tortuosity (Supplementary Fig. 5), consistent with a more efficient mass transport regime across the CL. These findings collectively suggest that the microscopic interface structure governs the porosity, gas access, and mass transport regime of the CL, ultimately dictating whether efficient 2e<sup>-</sup> ORR can be sustained under demanding conditions.

To clarify how microscale pore structures influence species transport, mesoscale simulations of gas-liquid-solid interactions within the CLs of FSE and PPE were performed. CL architectures were reconstructed using the QSGS method by tuning the PTFE nucleation

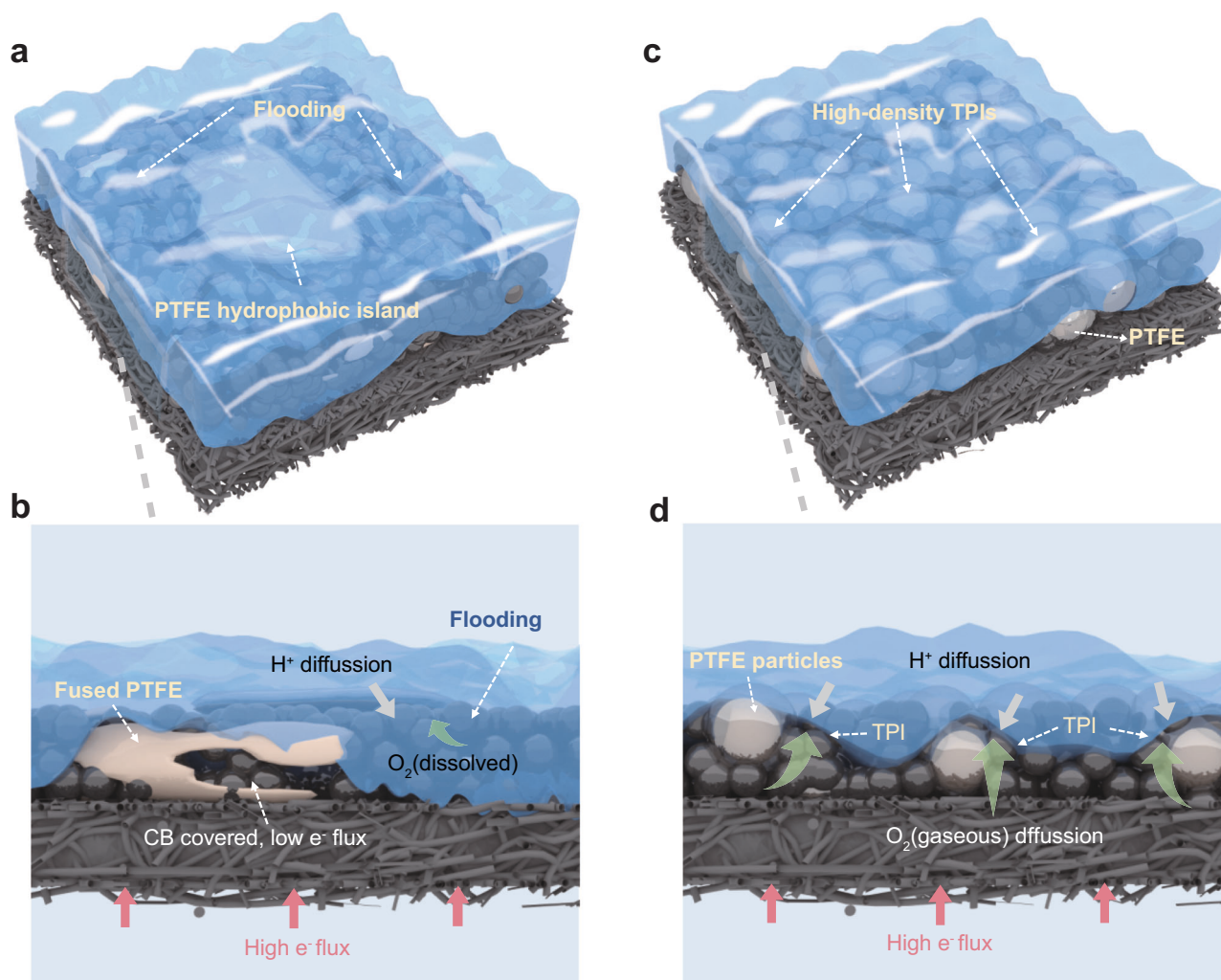


**Fig. 1 | Schematic comparison of conventional and particulate-packed CL structures and their impact on TPI formation.** **a** Conventional CL structure of a fused and segregated electrode (FSE), showing large agglomerated PTFE hydrophobic islands and extensive CB regions flooded with electrolyte. **b** Magnified side view of (a), illustrating a fused PTFE domain covering CB particles, while surrounding CB is immersed in the electrolyte and relies solely on dissolved oxygen for

$2e^-$  ORR, severely limiting TPI formation. **c** Catalyst layer with a non-fused particulate-packed interface (PPE), where PTFE and CB particles form a porous and interspersed network. **d** Magnified side view of **c**, where discrete PTFE particles create localized hydrophobic microenvironments that enable nearby CB to participate in  $2e^-$  ORR, resulting in abundant and uniformly distributed TPIs.

probability ( $P_c$ ) and phase occupation ratio ( $R_p$ ), mimicking PTFE structural evolution during fabrication (“Methods”)<sup>26,27</sup>. The reliability of the QSGS-generated structures was quantitatively validated by comparing their porosity and CB/PTFE volume ratio with those of the FIB-SEM reconstructed catalyst layer, showing good consistency (Supplementary Fig. 6). As shown in Supplementary Fig. 7, PTFE in the FSE CL aggregated into large domains, whereas in PPE, PTFE remained in discrete particulate form. Subsequent LBM simulations (details in Methods) captured the steady-state distribution of phases under liquid intrusion (Fig. 2g)<sup>28,29</sup>. Cross-sectional views revealed that in FSE, gas appeared near aggregated PTFE domains, turning PTFE into isolated hydrophobic islands while leaving CB submerged in electrolyte—explaining the drop in FE. In contrast, PPE’s particulate-packed structure formed alternating hydrophilic-hydrophobic zones, creating a percolating TPI network (Fig. 2h).

It should be noted that the above analysis mainly attributes the inferior performance of FSE to pore densification, while the intrinsic limitation associated with PTFE encapsulation of carbon particles has not been fully clarified. To decouple these two effects, a comparison electrode (PPE-cal) was prepared by calcining the spray-coated PPE at 340 °C without hot pressing. This treatment induced partial PTFE

melting and CB encapsulation while maintaining the same packing density as PPE, thereby isolating the influence of densification caused by hot pressing. As shown in Supplementary Fig. 8, PPE-cal exhibited partial PTFE fusion but lacked the compact morphology of FSE. Electrochemical  $H_2O_2$  synthesis revealed a clear performance hierarchy of PPE > PPE-cal > FSE, indicating that both molten encapsulation and reduced porosity contribute to the degraded performance of conventional electrodes (Supplementary Fig. 9). Similar binder-induced encapsulation effects have also been observed in ionomer-based catalyst layers (e.g., Nafion coatings on Pt/C), where excessive polymer coverage hinders gas diffusion, highlighting the broader relevance of this interfacial limitation<sup>30</sup>. These findings indicate that the microscopic interface architecture plays an important role in shaping pore morphology and mass-transport pathways, which in turn influence electrode performance at high current densities. (see detailed analysis below).

### CL optimization based on non-fused particulate interface architecture

Having identified the optimal interface architecture, we systematically varied the PTFE-to-CB mass ratio (P/C = 0–1.5, with fixed catalyst

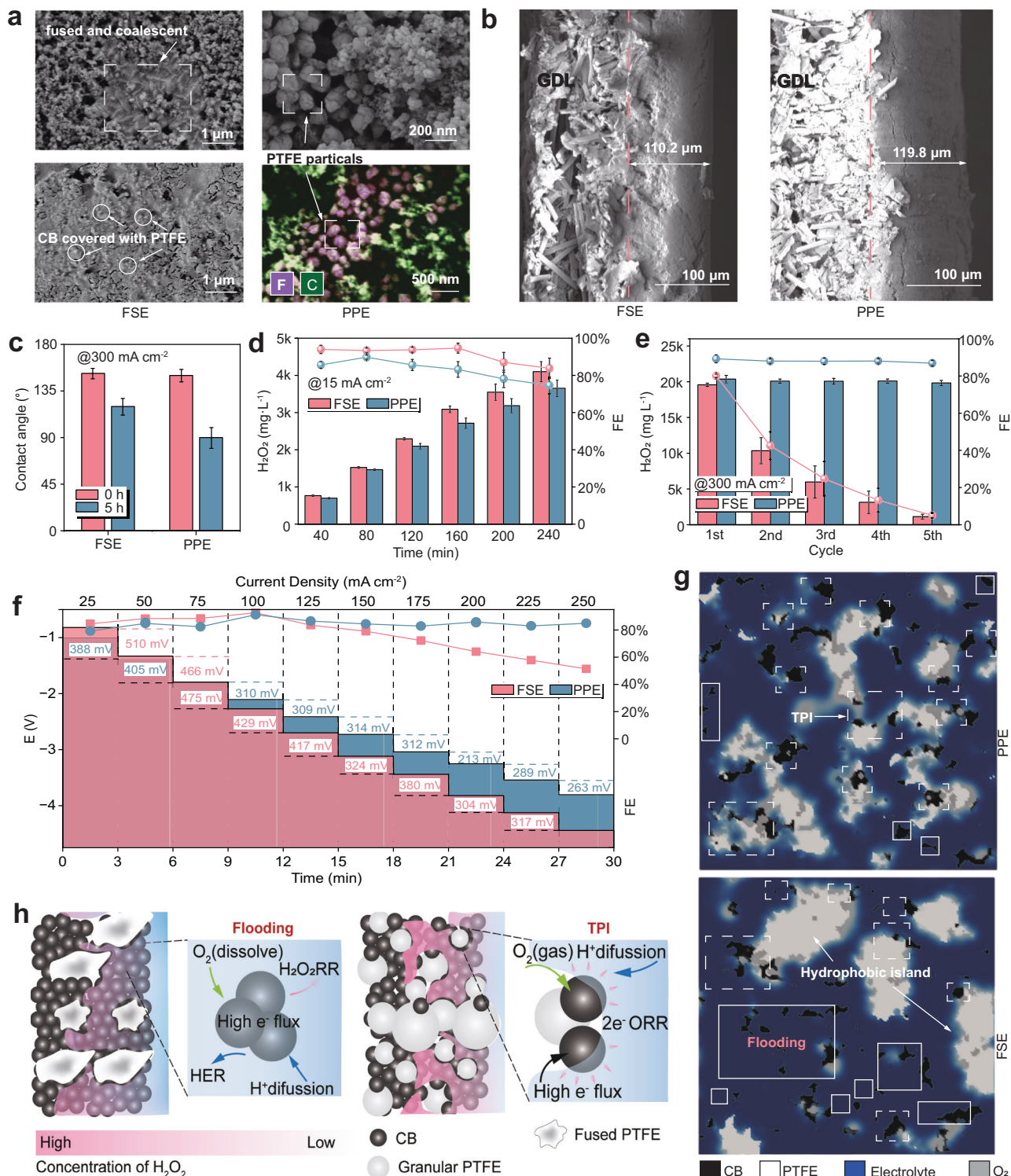


**Fig. 2 | Morphological and performance comparisons of two catalyst/binder interface structures.** **a** Microstructural characterization of catalyst/binder interfaces in FSE and PPE electrodes. **b** Cross-sectional SEM images of FSE and PPE. **c** Water contact angle evolution before electrolysis and after five consecutive cycles of electrolysis, 1 h per cycle. **d**  $\text{H}_2\text{O}_2$  yield and corresponding Faraday efficiency (FE) at 15  $\text{mA cm}^{-2}$  (0.1  $\text{mol L}^{-1}$   $\text{Na}_2\text{SO}_4$ , pH = 5.84  $\pm$  0.01, mass loading of 6  $\text{mg cm}^{-2}$ ). **e**  $\text{H}_2\text{O}_2$  yield and FE at 300  $\text{mA cm}^{-2}$  for five consecutive cycles, 1 h per cycle (1  $\text{mol L}^{-1}$   $\text{Na}_2\text{SO}_4$ , pH = 6.92  $\pm$  0.06, mass loading of 6  $\text{mg cm}^{-2}$ ). Values are means, and error bars indicate standard deviation ( $n = 3$  replicates). Source data are provided as a Source Data file. **f** Steady-state potential response and FE under

stepwise current loading (25–250  $\text{mA cm}^{-2}$ , 25  $\text{mA cm}^{-2}$  per 3 min step, 1  $\text{mol L}^{-1}$   $\text{Na}_2\text{SO}_4$ , pH = 6.92  $\pm$  0.06, mass loading of 6  $\text{mg cm}^{-2}$ ). Values are means ( $n = 3$ ). Full statistical information, including standard deviations and raw data, is provided in the Source Data file. **g** LBM-simulated gas-liquid-solid distribution in CLs with distinct interface structures. **h**  $\text{O}_2$  transport behavior and reaction process in the CL of FSE (left) and PPE (right). In FSE, the PTFE hydrophobic islands leads to widespread flooding of CB, forcing the  $2\text{e}^-$  ORR to rely solely on dissolved oxygen and increasing the likelihood of undesired  $\text{H}_2\text{O}_2$  reduction. In contrast, the interpenetrating network of PTFE and CB in PPE significantly enhances the number of accessible TPIS, promoting efficient oxygen transport and utilization.

loading) to tune the abundance and spatial distribution of non-fused particulate-packed interfaces. Electrolysis tests were conducted across 15–400 mA cm<sup>-2</sup> (Fig. 3a and Supplementary Fig. 10). Due to the fabrication method, even the PTFE-free electrode (P/C = 0) exhibited 80% and 60% FE at 15 and 100 mA cm<sup>-2</sup>, respectively—demonstrating performance that remains competitive with certain PTFE-containing systems reported in the literature.<sup>13,31,32</sup> However, CB oxidation in H<sub>2</sub>O<sub>2</sub>-rich environments gradually increases hydrophilicity, restricting O<sub>2</sub> access at higher currents<sup>31,33</sup>. Stepwise chronoamperometry confirmed this: P/C-0 showed large voltage deviation and rapid FE decline beyond 200 mA cm<sup>-2</sup>, indicating severe oxygen transport limitations and parasitic hydrogen evolution (Fig. 3b, c), consistent with the FE trend in Fig. 3a. In contrast, PTFE-containing GDEs maintained >80% FE and stable voltages up to 250 mA cm<sup>-2</sup> (Fig. 3a). This consistent performance contrasts with previous studies, which reported significant performance divergence even below 100 mA cm<sup>-2</sup> and within 1 h of operation<sup>6,11,12,34</sup>. These results reaffirm that particulate-packed interfaces promote full exposure of catalytic active sites, delivering consistent performance under low oxygen demand. At higher current densities, greater oxygen demand requires more PTFE to sustain hydrophobicity and gas transport, shifting optimal FE toward higher P/C ratios (Fig. 3a). LSV confirmed this trend: at low potentials, all electrodes responded similarly, with P/C-0 slightly higher due to enhanced ionic transport from its more hydrophilic surface. As potential increased, P/C-0 exhibited a clear deviation from linearity, with current growth slowing due to oxygen transport limitation, while P/C-0.9 maintained a linear response, reflecting improved O<sub>2</sub> access and overall performance (Fig. 3d).

Unexpectedly, the FE of P/C-1.2 and P/C-1.5 sharply declined to 69 and 41%, respectively, at 400 mA cm<sup>-2</sup> (Fig. 3a). We hypothesized that excessive hydrophobicity might hinder proton transport. To test this, Nafion was added to the ink to enhance proton conductivity; however, performance did not recover, ruling out proton transport as the limiting factor (Fig. 3a). In contrast, supplying external oxygen to the GD side restored the performance of P/C-1.5 to P/C-0.9 levels, confirming oxygen transport as the primary bottleneck. Paradoxically, P/C-1.5 would theoretically be expected to offer enhanced oxygen retention compared to P/C-0.9. This counterintuitive result suggests the presence of microscale limitations within the CL that override the bulk material properties. SEM images revealed clear spatial separation between PTFE and CB in P/C-1.5 (Fig. 3e). Such inhomogeneous distribution causes electrolyte to preferentially migrate toward CB-rich zones under surface tension, undermining the formation of effective triple-phase interfaces (Fig. 3f). Thus, oxygen transport and TPI stability are governed not merely by the amount of hydrophobic binder, but by its spatial localization within the CL.

To further investigate the origin of PTFE/CB separation at high P/C ratios, ink formulations were analyzed using a laser particle size analyzer<sup>35,36</sup>. As shown in Fig. 3e, increasing the P/C ratio shifted the particle size distribution toward larger diameters, with elevated D<sub>50</sub> and D<sub>90</sub> values (Supplementary Table 1). This indicates that higher PTFE content led to increased precipitation in the ink, which likely contributed to large PTFE agglomerates during CL fabrication<sup>17,37</sup>. While the impact of ink dispersion on fuel cell electrodes is well established<sup>38,39</sup>, such effects remain underexplored in H<sub>2</sub>O<sub>2</sub> electro-synthesis. In alcohol-based media, PTFE readily flocculates due to low surface energy and poor dispersion stability<sup>17</sup>. We found that elevated temperature, rapid PTFE addition, and high P/C ratios exacerbated flocculation, driven by strong interparticle attraction and bridging effects in neutral, nonionic solvents (Supplementary Fig. 11 and Supplementary Table 2)<sup>18,40</sup>. These results suggest that although particulate-packed structures benefit from increased PTFE content in theory, poor dispersion imposes a practical upper limit—one that may require advanced dispersion strategies to overcome.

## Mechanism of gas-liquid transport and TPI in CLs

To clarify how catalyst and binder co-assembly shapes internal pores and governs gas-liquid interactions, we combined 3D FIB-SEM reconstruction with mesoscale simulations to visualize and quantify internal fluid behavior. The real 3D structure of the CL was reconstructed via FIB-SEM (Supplementary Fig. 12), with two pretreatment protocols validated beforehand (Supplementary Note 1; Supplementary Figs. 13 and 14) to ensure structural integrity<sup>41,42</sup>. The reconstructed CL (Fig. 4a) reveals PTFE and CB as interspersed particulate aggregates, forming a packed granular network. PTFE appears as spheres or loose flocculates (10–100 nm, Supplementary Fig. 15). These 3D images confirm that PTFE and CB are interspersed as particulate ensembles, forming a packed granular architecture (Fig. 4b). Quantitative voxel-based analysis revealed the particle size, porosity, and pore size distribution of each component. The CL exhibited a bimodal solid-phase size distribution: CB was primarily found in the 0–50 nm range, consistent with its intrinsic size (~30 nm; Supplementary Fig. 16)<sup>43</sup>. The overall porosity (~0.73) aligned well with mercury intrusion data (Supplementary Fig. 17, and Fig. 2g). While micropores (<10 nm) dominated the pore population, as widely reported<sup>16</sup>, our CLs contained a significantly higher fraction of meso- and macropores, which are more favorable for O<sub>2</sub> and H<sub>2</sub>O<sub>2</sub> transport.

After obtaining the 3D structure of the real CL, we simulated gas-liquid-solid three-phase flow using the LBM<sup>29,44</sup>. In these simulations, the electrolyte was treated as an ideal, incompressible, charge-neutral fluid. Although this simplification neglects ionic strength and electrostatic effects, it captures the capillary-driven intrusion dominated by pore geometry and wettability at the mesoscale. Similar assumptions are widely used in multiphase-flow models of porous electrodes for fuel cells, validating its suitability for describing gas-liquid dynamics in GDEs<sup>29</sup>. To avoid the non-physical interfacial film artifacts commonly encountered in traditional pseudopotential models near solid surfaces, we adopted a recently developed phase-field model and implemented it on a GPU-accelerated CUDA platform (simulation parameters in Supplementary Table 3)<sup>45,46</sup>. The physical model and boundary conditions are shown in Supplementary Fig. 15. Figure 4c presents a YZ cross-section at  $x=110$  (Supplementary Fig. 18). The visualization clearly reveals that isolated hydrophilic CB domains are rapidly infiltrated by the electrolyte. In contrast, regions where PTFE and CB coexist support the formation of TPI, underscoring that sharp wettability contrast is a prerequisite for TPI formation. Additionally, some CB-only pores resist flooding, suggesting geometry and wettability co-govern TPIs development. 3D renderings (Supplementary Fig. 19) further show that intrusion occurs through finger-like pathways rather than uniform fronts, characteristic of capillary-driven flow<sup>47</sup>. Local wettability gradients at CB/PTFE interfaces trap air pockets of various sizes, fostering stable TPIs. Figure 4d shows that as intrusion proceeds, gas-liquid interfaces proliferate and interconnected air channels form, enabling efficient O<sub>2</sub> transport. Notably, even after the electrolyte exits the domain at timestep 170,000, gas pockets persist through timestep 200,000 (see Supplementary Movie 1). We quantified this behavior by tracking time-resolved liquid saturation (Supplementary Fig. 20), confirming that part of the pore volume remains consistently gas-filled at steady state<sup>48</sup>. These findings capture the ways in which electrolyte transport can be guided by pore geometry and wettability gradients rather than being entirely random. This directional control marks a paradigm shift—from blocked to guided transport—and provides a theoretically sound route for constructing durable and efficient triple-phase interfaces.

To assess the feasibility of guiding electrolyte transport through structural regulation, the QSGS algorithm was used to generate CL structures by tuning nucleation probability ( $P_c$ ) and phase occupation ratio ( $R_p$ ), and gas-liquid behavior was quantified via LBM. Structures 1–3 shared similar PTFE dispersion but progressively increased PTFE content and decreased porosity by raising  $R_p$ . Structures 2, 4, and 5

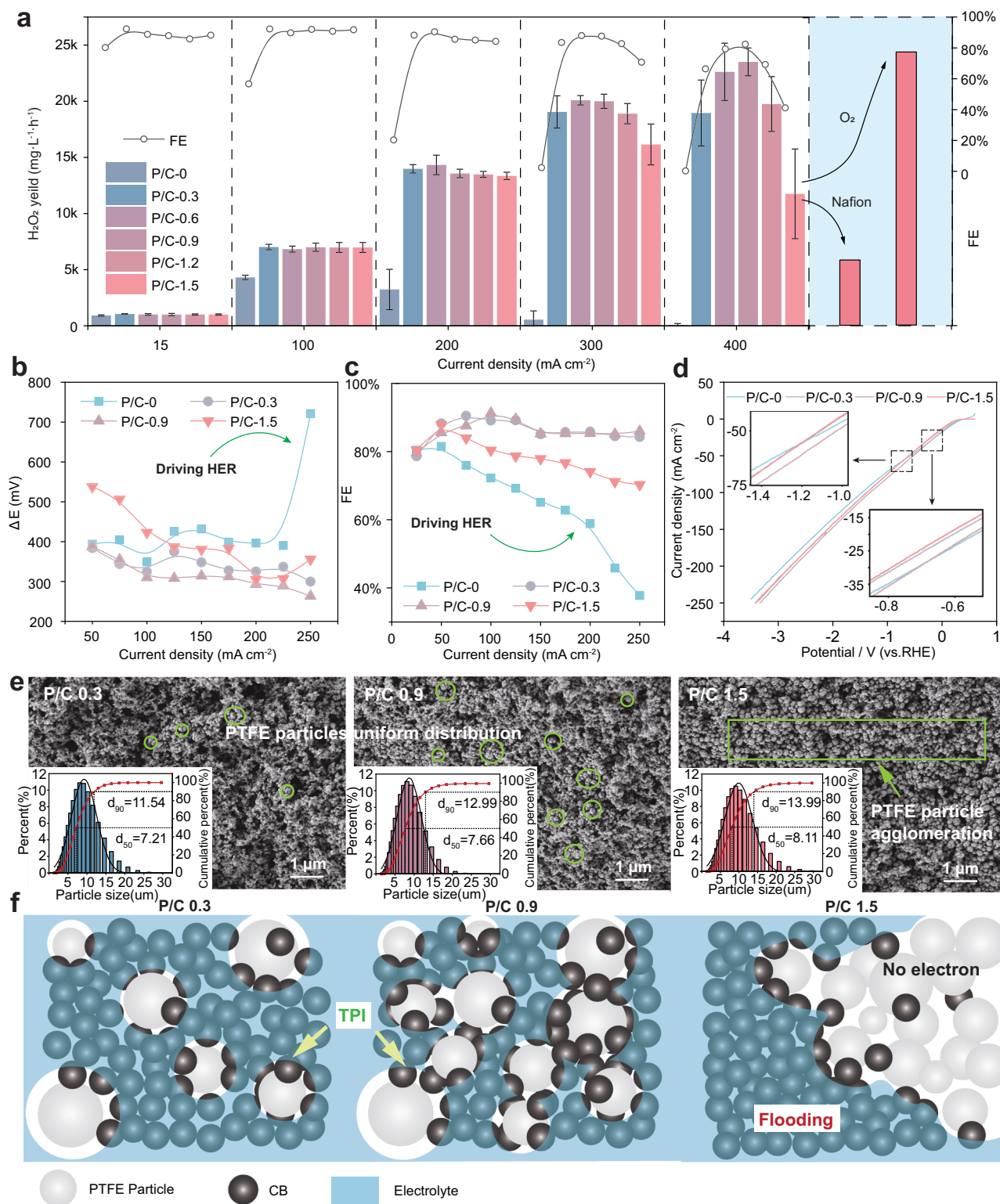
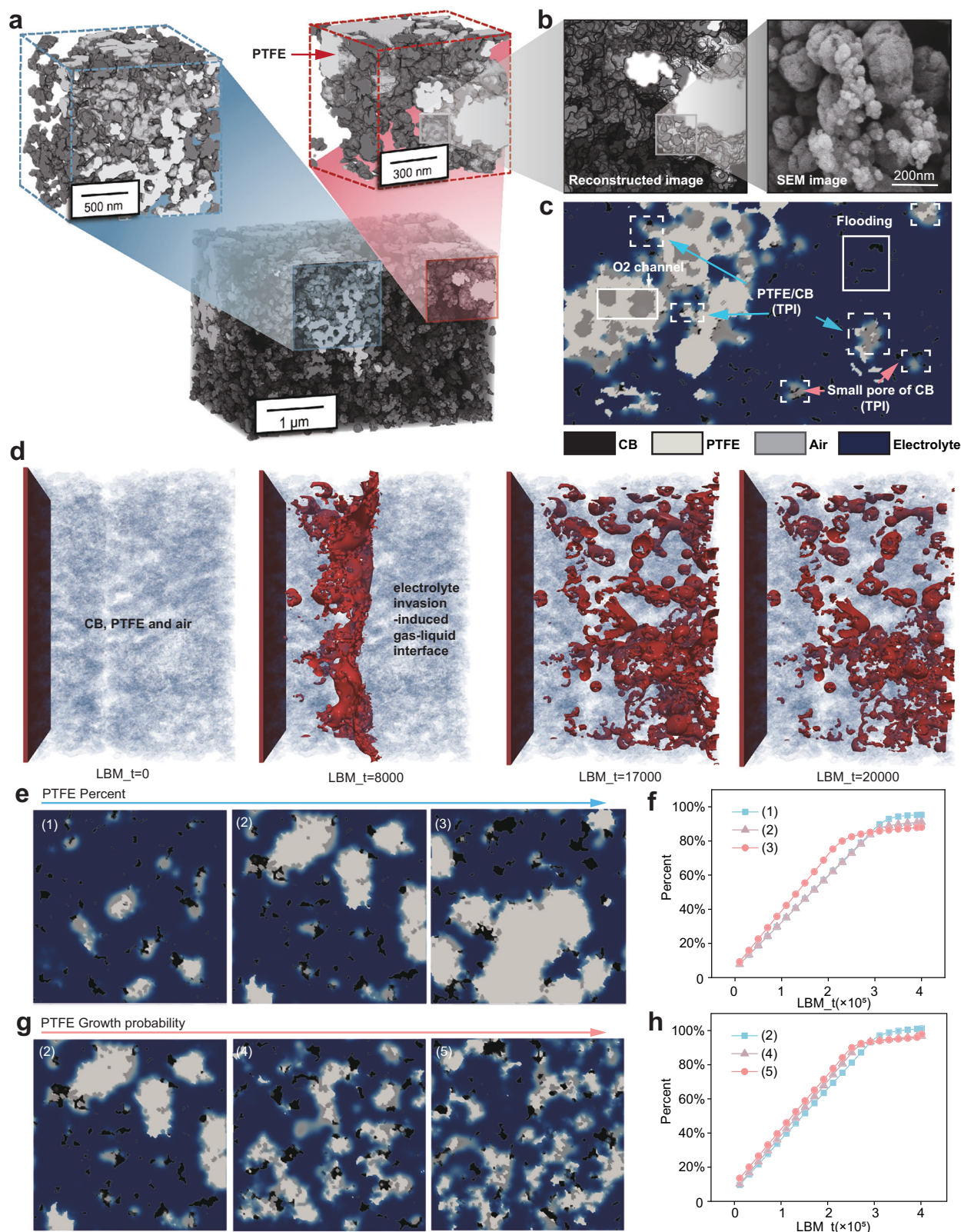


**Fig. 3 | Electrochemical performance and ink properties of GDEs with different PTFE/CB ratios. a**  $\text{H}_2\text{O}_2$  yield and corresponding Faraday efficiency (FE) at different current densities (Tests at 15 and 100  $\text{mA cm}^{-2}$  were conducted in  $0.1 \text{ mol L}^{-1} \text{ Na}_2\text{SO}_4$ ,  $\text{pH} = 5.84 \pm 0.01$ , while tests at 200, 300, and 400  $\text{mA cm}^{-2}$  were carried out in  $1 \text{ mol L}^{-1} \text{ Na}_2\text{SO}_4$ ,  $\text{pH} = 6.92 \pm 0.06$ ). “O<sub>2</sub>” indicates operation with external oxygen supply to replace the self-breathing mode; “Nafion” refers to electrodes with additional Nafion binder incorporated into the CL. Values are means, and error bars indicate standard deviation ( $n = 15$  replicates). **b** Steady-state potential response

and **c** FE under stepwise current loading. Values are means, and error bars indicate standard deviation ( $n = 3$  replicates). **d** LSV curves for different GDEs with different PTFE/CB ratios (mass loading of  $6 \text{ mg cm}^{-2}$ , scan rate:  $20 \text{ mV s}^{-1}$ ,  $1 \text{ mol L}^{-1} \text{ Na}_2\text{SO}_4$ ,  $\text{pH} = 6.92 \pm 0.06$ , without  $iR$  compensation,  $iR = 4.55 \pm 0.6 \Omega$ ). **e** SEM images of different CLs with particle size distribution of inks with varying PTFE/CB mass ratios. **f** Diagrammatic sketch of different CLs with varying PTFE/CB mass ratios. Source data are provided as a Source Data file.



maintained constant PTFE content while increasing spatial uniformity through higher  $P_c$  (Supplementary Fig. 21; Supplementary Tables 4 and 5). LBM simulations showed that increasing PTFE content (structures 1–3) reduced electrolyte saturation—suggesting that lower porosity can effectively impede water intrusion (Fig. 4e, f). However, increased PTFE content failed to alleviate CB flooding or enhance TPI formation—a finding that rationalizes why excessive PTFE loading in

prior studies failed to improve electrode performance. In structure 3, PTFE aggregation and segregation further accelerated catalyst flooding, further explaining performance decline at high PTFE loadings (Supplementary Figs. 22 and 23). In contrast, improving PTFE dispersion at constant content (structures 2, 4, and 5) significantly increased the spatial density of gas-liquid-solid interfaces (Fig. 4g and Supplementary Fig. 24) and formed more dense and continuous gas networks

**Fig. 4 | Three-dimensional reconstruction of catalyst layers revealing gas-liquid transport dynamics and TPI development.** **a** Real 3D structure of the catalyst layer (CL) reconstructed by FIB-SEM, showing the spatial distribution of CB and PTFE. **b** Magnified local view of the CL, where CB particles are attached to aggregated PTFE domains; corresponding SEM image is provided for comparison. **c** Gas-liquid-solid configurations captured during electrolyte invasion via LBM simulations. **d** Evolution of gas-liquid interfaces within the CL over time, highlighting bubble formation and distribution during progressive electrolyte penetration.

**e** Gas-liquid-solid distributions obtained from LBM simulations for catalyst layer structures with increasing PTFE content, denoted as structures 1–3. **f** Corresponding liquid saturation levels in the catalyst layers shown in **e**, illustrating reduced electrolyte intrusion with increasing PTFE content. **g** Gas-liquid-solid distributions for catalyst layer structures with identical PTFE content but different PTFE dispersion uniformity, denoted as structures 2, 4, and 5, where the spatial distribution of PTFE becomes progressively more uniform. **h** Corresponding liquid saturation levels in the catalyst layers shown in **g**.

(Supplementary Fig. 25), underscoring ink dispersion quality as a key performance factor. Notably, liquid saturation remained largely unchanged across these, suggesting porosity and PTFE content are the dominant factor governing electrolyte penetration (Fig. 4h). To clarify the mechanism of TPI formation, we modeled pores with varied wettability and geometry (Supplementary Fig. 26). As shown in Supplementary Fig. 27, phase separation occurred mainly in pores bordered by contrasting wettability, where asymmetrical capillary forces drove water to hydrophilic regions, stabilizing gas in hydrophobic domains—thereby stabilizing TPIs. Furthermore, pore size played a decisive role: small hydrophobic pores significantly delayed water invasion, consistent with our earlier saturation–porosity analysis, while smaller hydrophilic pores accelerated it. Together, these findings indicate that gas-liquid dynamics are jointly governed by pore morphology and wettability—offering critical guidance for rational TPI design.

### Hierarchical gradient CL for liquid repellence and guided product transport

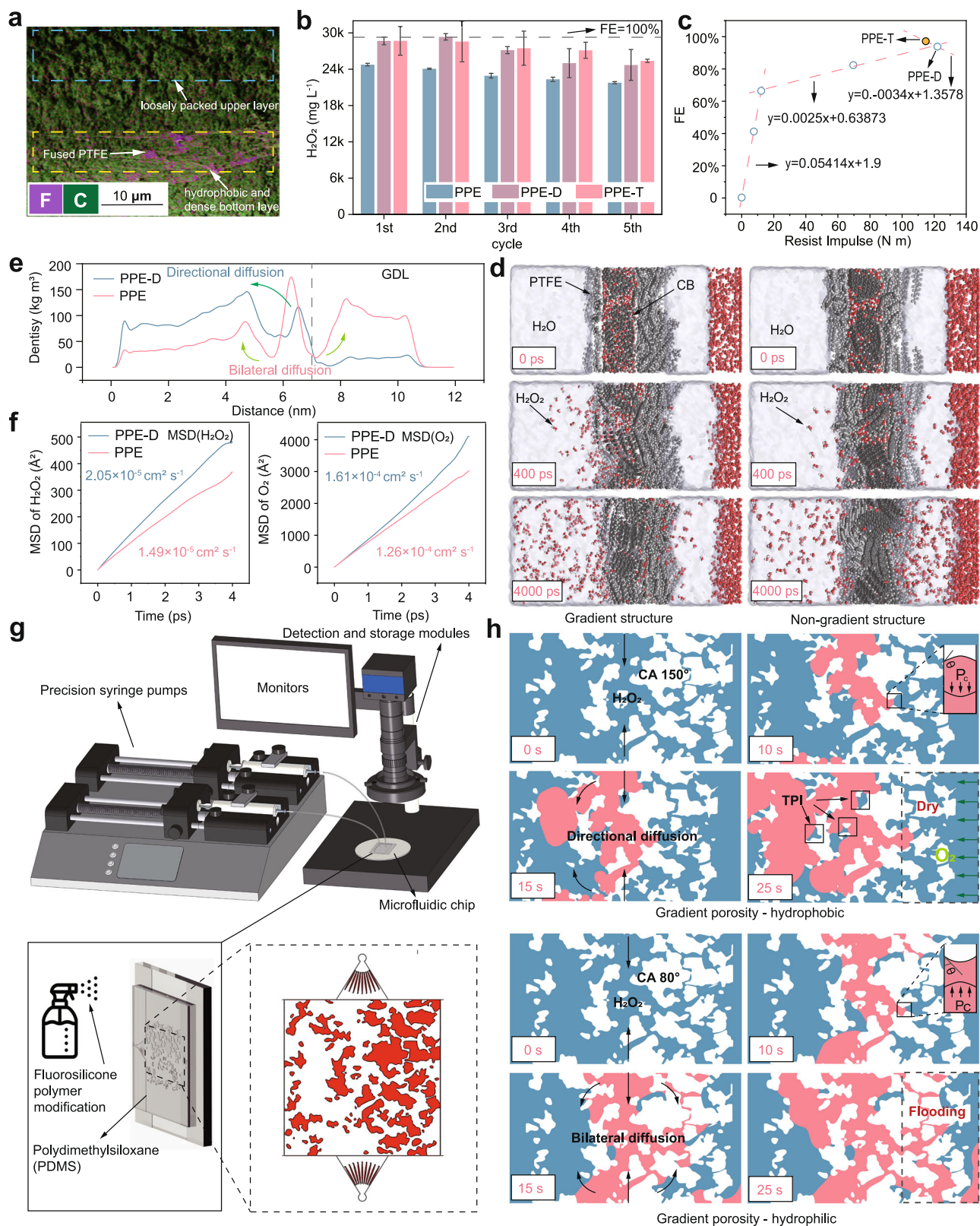
Building on previous findings, a hierarchically structured CL with porosity and wettability gradients was designed to guide electrolyte transport. To systematically assess the influence of gradient design, we fabricated electrodes with dual-layer (PPE-D) and triple-layer (PPE-T) gradient architectures in addition to a single-layer reference (PPE). For PPE-D, a PTFE-rich ink was first coated onto the gas diffusion layer (GDL) and sintered to form a dense, highly hydrophobic layer with fine pores, serving as the first CL<sup>49</sup>. A second catalyst layer composed of non-fused particulate packing was then deposited on top, yielding a dual-gradient structure (PPE-D) with controlled PTFE content (1.8–3.6 mg cm<sup>-2</sup>) (Supplementary Fig. 28). Cross-sectional EDS mapping (Fig. 5a) qualitatively confirmed that the bottom layer is denser and richer in fused PTFE, establishing a clear porosity gradient. Mercury intrusion porosimetry (Supplementary Fig. 29) quantitatively confirmed a porosity gradient, with a marked decrease in pore volume toward the PTFE-rich bottom layer, consistent with densification and partial pore blockage from sintering. Because contact-angle measurements are unreliable for rough porous surfaces, PTFE loading was used as a quantitative indicator of hydrophobicity. The higher PTFE content in the bottom layer indicates stronger electrolyte repellence, confirming coupled porosity–wettability gradients across the CL.

For PPE-T, while adding another low-PTFE catalyst layer could further steepen the gradient, such multilayer assembly would complicate fabrication and hinder scalability. Instead, oxygen plasma etching provides a rapid, controllable, and catalyst-independent approach to tune surface hydrophilicity without additional coating or structural damage<sup>50</sup>. We therefore applied plasma etching to PPE-D, enabling a simple and scalable enhancement of surface wettability. The treatment introduces oxygenated groups (–OH, C=O, C–O–C) that raise surface energy and reduce the top-layer contact angle from 158° to 30° (Supplementary Fig. 30). XPS and EDS analyses verified the incorporation of these oxygenated groups, and the plasma parameters were optimized to preserve catalyst activity and pore morphology (Supplementary Fig. 31–33). The resulting electrode, PPE-T, thus exhibits a continuous porosity–wettability gradient throughout the CL.

We next compared the performance of PPE, PPE-D, and PPE-T to evaluate the effect of gradient steepness. The dual-gradient design (PPE-DL8) maintained 83% FE after 5 h—43% higher than PPE (Fig. 5b and Supplementary Fig. 34). The same performance hierarchy of FSE < PPE < PPE-D was maintained under both acidic and alkaline electrolytes, confirming that the structural design principles are generally applicable across different pH environments (Supplementary Fig. 35). The introduction of a surface-modified hydrophilic layer further amplified this effect: PPE-T outperformed both PPE and PPE-D, maintaining nearly 100% FE during the first 3 h (Fig. 5b). Across 0–500 mA cm<sup>-2</sup>, PPE-T exhibited a near-linear increase in H<sub>2</sub>O<sub>2</sub> production rate, consistent with reduced oxygen-transport limitations (Supplementary Fig. 36). These results demonstrate that introducing multi-layered wettability gradients via scalable surface modification strategies can substantially enhance GDE performance under practical operating conditions.

To elucidate the origin of the performance enhancement, LBM simulations were combined with in situ experiments to assess electrolyte breakthrough behavior. Gradient and non-gradient structures were generated using a modified QSGS algorithm (Supplementary Fig. 37). The simulations showed that, at the same timestep, PPE-D restricted electrolyte intrusion to localized gas-liquid regions, preserving oxygen pathways, whereas PPE was completely flooded (Supplementary Fig. 38). These trends were further verified by in situ breakthrough pressure tests (Supplementary Fig. 39). Under constant mechanical load and applied potential, the time required for peroxide test paper on the GDL to show discoloration was recorded (Supplementary Fig. 40). Multiplying the applied pressure by breakthrough time yielded the resistance impulse (RI), a quantitative indicator of intrinsic flooding resistance. The RI values of all electrodes were compared to evaluate their flooding resistance (Supplementary Fig. 41). Both PPE-D and PPE-T exhibited significantly higher RI than PPE, confirming their resistance to electrolyte intrusion under electro-wetting and explaining their improved performance. Further analysis of the relationship between FE and RI (Fig. 5c) revealed two distinct regimes: in the low-RI range, FE rose steeply with increasing RI (slope = 0.054), reflecting the positive contribution of enhanced hydrophobicity; beyond a critical RI, the increase plateaued (slope = 0.0025), suggesting that the barrier effect alone had approached its limit. Notably, PPE-T deviated from this linear correlation—its RI decreased, yet its FE increased significantly. This deviation suggests that, in addition to passive flooding resistance, an extra transport behavior may have emerged, potentially associated with the steeper wettability gradient. To further separate these effects, additional electrolysis experiments were performed by floating PPE and PPE-T horizontally on the electrolyte surface without any applied hydrostatic pressure, thereby minimizing the influence of breakthrough pressure. Even under pressure-free conditions, PPE-T maintained a higher FE than PPE (Supplementary Fig. 42), confirming that observed performance enhancement cannot be solely attributed to passive barrier protection. Instead, it likely results from a synergistic interplay between passive anti-flooding resistance and additional gradient-induced mass transport.

To further elucidate this behavior, LBM and molecular dynamics (MD) simulations were subsequently conducted to analyze the in situ diffusion of H<sub>2</sub>O<sub>2</sub> within the CL at mesoscale and molecular scales,



respectively. The LBM simulations revealed that  $\text{H}_2\text{O}_2$  spontaneously migrates toward regions with larger pores and lower PTFE content, thereby preserving dry domains that maintain access to oxygen (Supplementary Fig. 43 and Supplementary Movie 2). To quantify this effect, MD simulations were conducted to calculate mass-transfer coefficients (Supplementary Fig. 44 and Fig. 5d)<sup>23</sup>. Despite identical PTFE content, the gradient CL exhibited directional  $\text{H}_2\text{O}_2$  diffusion

with a transport coefficient of  $2.05 \times 10^{-5} \text{ cm}^2 \text{ s}^{-1}$ , 37.6% higher than the bidirectional diffusion observed in the non-gradient system ( $1.49 \times 10^{-5} \text{ cm}^2 \text{ s}^{-1}$ , Fig. 5e, f). Simultaneously, the removal of  $\text{H}_2\text{O}_2$  facilitated  $\text{O}_2$  diffusion into the CL, increasing its mass-transfer coefficient from  $1.26 \times 10^{-4}$  to  $1.61 \times 10^{-4} \text{ cm}^2 \text{ s}^{-1}$  (a 27.8% improvement). These enhancements suppress local  $\text{H}_2\text{O}_2$  accumulation and promote  $\text{O}_2$  replenishment at the TPI. While the LBM and MD simulations

**Fig. 5 | Gradient wettability and structural hierarchy promote directional transport and enhance electrode performance.** **a** Cross-sectional EDS mapping results of PPE-D featuring a dense hydrophobic bottom layer and a particulate-packed top layer, forming a structural and wettability gradient. **b** H<sub>2</sub>O<sub>2</sub> yield and corresponding Faraday efficiency (FE) for different GDEs (1 mol L<sup>-1</sup> Na<sub>2</sub>SO<sub>4</sub>, pH = 6.92 ± 0.06, mass loadings: PPE, 6 mg cm<sup>-2</sup>; PPE-D and PPE-T, 8 mg cm<sup>-2</sup>). Values are means, and error bars indicate standard deviation (*n* = 3 replicates). Source data are provided as a Source Data file. **c** Correlation between FE and the resistance impulse (RI) (1 mol L<sup>-1</sup> Na<sub>2</sub>SO<sub>4</sub>, pH = 6.92 ± 0.06). Values are means (*n* = 3). Full statistical information, including standard deviations and raw data, is provided in the Source Data file. **d** Molecular dynamics rendering of H<sub>2</sub>O<sub>2</sub> diffusion trajectories within gradient versus non-gradient CLs. **e** Time-resolved spatial density

distributions of H<sub>2</sub>O<sub>2</sub> molecules, showing preferential migration toward regions with larger pores and lower PTFE content in the gradient structure. **f** Mean square displacement (MSD) of H<sub>2</sub>O<sub>2</sub> and O<sub>2</sub> molecules in gradient and non-gradient CLs, indicating enhanced directional transport in the presence of wettability gradients. **g** Schematic of the microfluidic device designed to visualize directional H<sub>2</sub>O<sub>2</sub> flow in biomimetic CL channels. **h** Experimental visualization of H<sub>2</sub>O<sub>2</sub> transport in microfluidic chips with hydrophobic and hydrophilic gradients. The H<sub>2</sub>O<sub>2</sub> solution (mixed with potassium titanyl oxalate) appears pink and is injected from the central region. Pores are shown in blue and the solid skeleton in white. The observed capillary-driven directional transport is consistent with the CL gradient design (See Supplementary Videos 3 and 4 for experimental details).

capture the qualitative influence of pore architecture and wettability contrast on electrolyte intrusion and product transport, they do not fully reproduce the complexity of real electrochemical interfaces, including reaction kinetics, ion transport, and surface heterogeneity. The simulation results should therefore be interpreted as mechanistic insights rather than quantitative predictions. Since real-time nanoscale electrochemical imaging remains challenging, we developed a custom PDMS-based microfluidic visualization platform (2 × 2 cm) incorporating QSGS-derived gradient pore structures with fluorosilane-treated frameworks mimicking PTFE hydrophobicity (Fig. 5g)<sup>51</sup>. A potassium titanyl oxalate solution containing H<sub>2</sub>O<sub>2</sub> was injected into the chip center to simulate in situ product generation. Visualization experiments (Supplementary Movie 3 and 4) showed that, in the hydrophobic gradient chip, H<sub>2</sub>O<sub>2</sub> consistently migrated toward the large-pore region, leaving the small-pore side dry. Convex menisci at narrow throats indicated capillary barriers generating a net Laplace force that drove fluid directionally. In contrast, the hydrophilic gradient chip displayed symmetric diffusion and rapid flooding. These results highlight the critical role of wettability and pore gradients in directing mass transport and maintaining TPI integrity. Taken together, these findings reveal two synergistic yet distinct mechanisms that jointly govern electrode stability and efficiency: the dense hydrophobic sub-layer serves as a passive barrier that resists electrolyte intrusion, while the wettability gradient actively drives directional product evacuation and sustains TPIs under dynamic operation.

### Milestone demonstration of a commercial-scale self-breathing electro-synthesis platform

Electrode durability under harsh conditions remains a key barrier to industrial translation. The long-term stability of PPE-T without external aeration was evaluated across various current densities. To avoid thermal artifacts (Supplementary Fig. 45), the electrolyte was periodically replaced—every 4 h at low current and every 1 h at high current—without any electrode cleaning or hydrophobic regeneration, preserving realistic operational conditions. PPE-T maintained 90% FE over 500 h at 15 mA cm<sup>-2</sup>, producing 0.4 wt% H<sub>2</sub>O<sub>2</sub> per cycle. At 300 mA cm<sup>-2</sup>, it stably delivered 3 wt% H<sub>2</sub>O<sub>2</sub> h<sup>-1</sup> for 300 h at 85% FE—meeting the requirements of most industrial water treatment applications. Even at the extreme current density of 400 mA cm<sup>-2</sup>, PPE-T sustained 80% FE for 50 h (Fig. 6a, where the slight FE drop after 45 h likely arises from partial flooding in the catalytic layer, which could be mitigated by further optimizing the pore gradient and PTFE distribution). A benchmarking analysis against recent literature is provided in Supplementary Table 6, showing that our electrode delivers performance competitive with H<sub>2</sub>O<sub>2</sub> electro-synthesis systems reported over the past decade under similar operating conditions<sup>10–13,15,22,31,32,49,52</sup>. To enhance scalability, we transitioned from lab-scale batch cells to a modular, oxygen-fed flow-through electrolyzer (Supplementary Fig. 46), incorporating a dual-membrane solid-state electrolyte. This system enabled continuous production of high-purity H<sub>2</sub>O<sub>2</sub> (9000–19,000 mg L<sup>-1</sup>) across 80–240 mA cm<sup>-2</sup> at 4–10 V (Supplementary Fig. 47). The production cost was as low as \$1.1 kg<sup>-1</sup>, with a single-

stack capital cost of \$81.2. This low capital requirement stands in stark contrast to the substantial investments needed for conventional anthraquinone facilities, making this approach especially promising for distributed and scalable deployment (Supplementary Note 2).

Building on the demonstrated durability of PPE-T, we developed a pilot-scale self-breathing H<sub>2</sub>O<sub>2</sub> electro-synthesis platform (Fig. 6b). A modular stack comprising four serially connected electrolyzers (100 cm<sup>2</sup> GDE each) was integrated with electronic, fluidic, and thermal management subsystems, forming a commercially viable in situ H<sub>2</sub>O<sub>2</sub> platform (Fig. 6c and Fig. 6d). Operating under alkaline conditions, the system maintained 85–95% FE at 100 mA cm<sup>-2</sup> for over 100 h (Fig. 6e). Notably, this stability was achieved despite electrolyte pumping-induced dynamic pressure, which typically accelerates flooding in open, non-pressurized systems—a challenge widely acknowledged in recent literature<sup>33</sup>. Under these demanding conditions, the sustained efficiency underscores the reliable performance and operational stability of our electrode design. Crucially, eliminating the need for pure oxygen supply simplifies system integration and reduces both capital and spatial demands. With a production cost of \$0.381 kg<sup>-1</sup> and an installation footprint under 4 m<sup>2</sup>, the system achieves competitive economic and spatial performance compared with recently reported values (e.g., \$0.398 kg<sup>-1</sup>)<sup>8</sup>. This work presents an integrated self-breathing GDE-based H<sub>2</sub>O<sub>2</sub> electro-synthesis system operated at pilot scale, demonstrating the feasibility of translating laboratory concepts into practical operation. The platform highlights the potential of decentralized and sustainable peroxide production for future industrial implementation.

## Discussion

In this work, we present a rationally designed GDE architecture that integrates wettability engineering, pore structure modulation, and gradient CL design. The resulting self-breathing electrode sustains industrial-level current densities without the need for an external oxygen supply. Through 3D reconstruction, multiscale simulations, and visualization technology, we reveal that the synergy between interfacial wettability and pore architecture governs electrolyte intrusion and product transport pathways—offering a structural blueprint for optimizing GDE performance. The dual- and triple-layer configurations demonstrate enhanced FE and long-term durability over 500 h across a range of current densities. To scale up this architecture, we assembled a 400 cm<sup>2</sup> modular four-cell flow-through cell stack, integrated with fluidic, thermal, and electronic control systems. Operating at low energy cost (\$0.381 kg<sup>-1</sup> H<sub>2</sub>O<sub>2</sub>), the system continuously produces H<sub>2</sub>O<sub>2</sub>, showcasing a milestone demonstration of commercial-scale, self-breathing electro-synthesis. This study not only establishes design principles for next-generation GDEs but also marks a critical step toward the industrial deployment of electrochemical hydrogen peroxide synthesis.

## Methods

### Chemicals and materials

Carbon black (Vulcan XC-72R) was obtained from Cabot Corporation. A 60 wt% PTFE dispersion was provided by Guangdong Canrd New

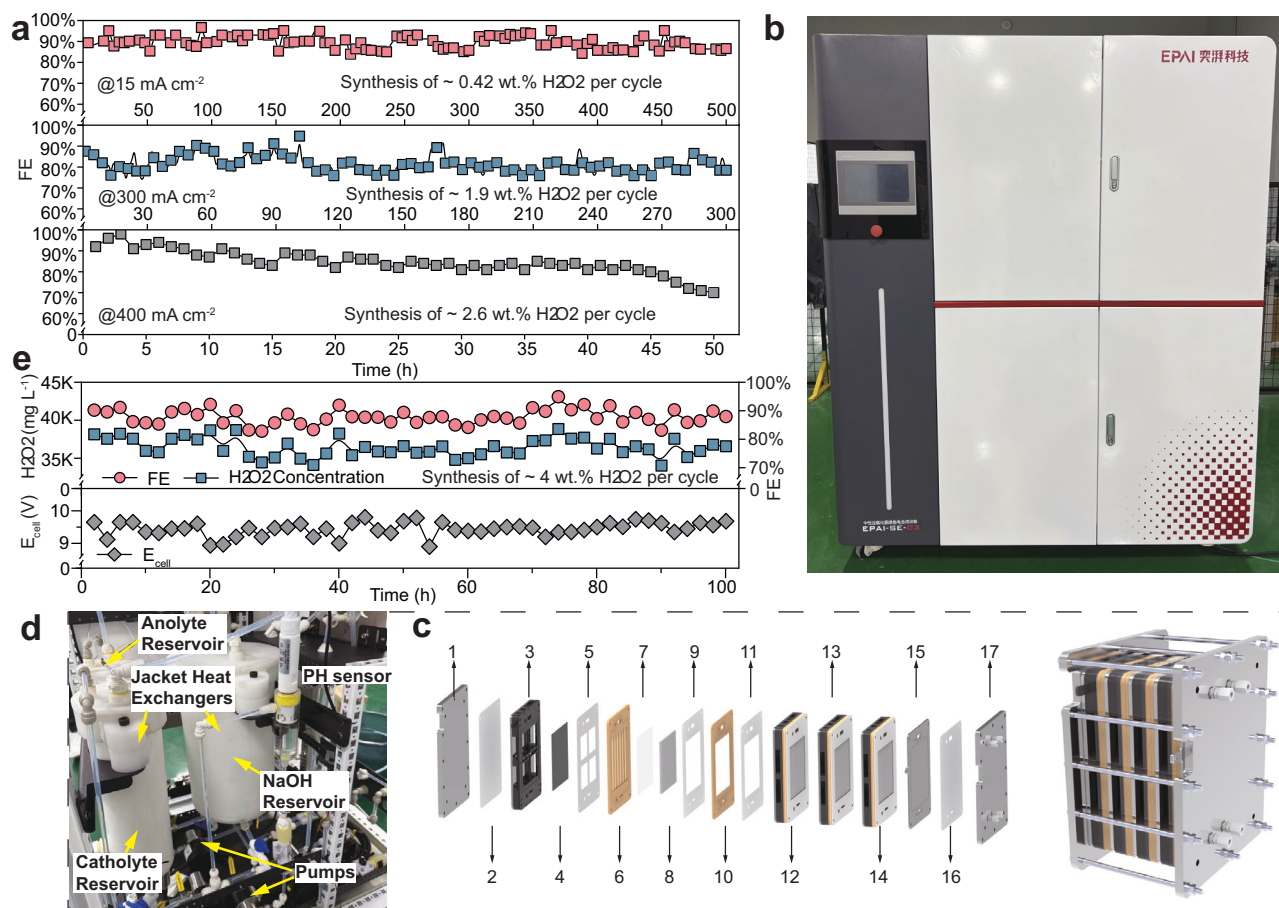


**Fig. 6 | Industrial validation and scale-up of self-breathing electrodes under demanding conditions.** **a** Long-term stability of PPE-T at 15, 300, and 400 mA cm<sup>-2</sup> (Tests at 15 and 100 mA cm<sup>-2</sup> were conducted in 0.1 mol L<sup>-1</sup> Na<sub>2</sub>SO<sub>4</sub>, pH = 5.84 ± 0.01, while tests at 200, 300, and 400 mA cm<sup>-2</sup> were carried out in 1 mol L<sup>-1</sup> Na<sub>2</sub>SO<sub>4</sub>, pH = 6.92 ± 0.06, mass loading of 8 mg cm<sup>-2</sup>). **b** Photograph of a fully integrated, pilot-scale electrolyzer system with four serially connected cells, incorporating electronic, fluidic, and thermal subsystems. **c** Exploded schematic of the four-cell modular stack. Key components include: 1/17, end plates; 2/5/9/11/16, silicone gaskets; 3, multifunctional bipolar plate enabling both self-breathing and structural support; 4, self-breathing GDE; 6, cathode flow plate; 7, proton-exchange membrane; 8, anode; 10, anode flow plate; 12–14, serially connected electrochemical

cells, each assembled from components 3–11; 16, anode current collector. **d** Internal view of the fluid and thermal management subsystem within the H<sub>2</sub>O<sub>2</sub> electro-synthesis platform. The platform comprises anodic and cathodic circulation loops driven by peristaltic pumps, using 5 mol L<sup>-1</sup> NaOH (anolyte, pH = 14 ± 0.02) and deionized water (catholyte). Each loop integrates flow, pressure, and level/pH monitoring. Electrolyte temperature is regulated by built-in water-jacket heat exchangers in both reservoirs. A modular power supply is mounted above the unit (not shown). **e** Long-term stability of the scaled system. Electrolysis was operated at 100 mA cm<sup>-2</sup> under ambient-pressure self-breathing conditions. Each durability test was performed once.

Energy Technology Co., Ltd. Carbon paper (TGP-H-060), a cation exchange membrane (Fumasep FKB-PK-130, 50 × 50 mm × 130 μm), and 5 wt% Nafion solution (D520) were purchased from Suzhou Sinero Technology Co., Ltd. Ti/IrO<sub>2</sub>-Ta<sub>2</sub>O<sub>5</sub> plates were supplied by Suzhou Shuertai Industrial Technology Co., Ltd. Sodium sulfate (Na<sub>2</sub>SO<sub>4</sub>, ≥99.0%, AR), sulfuric acid (H<sub>2</sub>SO<sub>4</sub>, 98%, AR), isopropanol (≥99.7%, AR), and sodium hydroxide (NaOH, ≥96%, AR) were purchased from China National Pharmaceutical Group Co., Ltd. Potassium titanium(IV) oxalate (K<sub>2</sub>TiO(C<sub>2</sub>O<sub>4</sub>)<sub>2</sub>, ≥98%) was also obtained from Macklin. Unless otherwise stated, all reagents were of analytical grade. The cation exchange membrane was used to separate the catholyte and anolyte. Before use, the membrane was soaked in 0.5 mol L<sup>-1</sup> NaCl at 25 °C for 24 h and rinsed with deionized water. All electrolytes were prepared freshly before each experiment and used immediately without further purification.

#### Fabrication of different cathodes

**Fused-coated electrode with segregated interface (FSE):** To prepare the FSE electrode with a conventional fused PTFE/CB interface, 150 mg of CB was dispersed in isopropanol/deionized water and sonicated for

5 min. PTFE emulsion (PTFE/CB = 0.9) was added dropwise under continuous sonication. The mixture was sonicated at 70 °C until a paste formed and coated onto carbon paper (CP), which served as both the current collector and gas diffusion layer. The electrode was hot-pressed at 10 MPa and 60 °C for 5 min, then annealed at 340 °C for 1 h.

**Particulate-packed electrode (PPE):** For the non-fused particulate interface structure, 150 mg of CB was dispersed in 10 ml isopropanol and sonicated for 5 min at 10 °C. A specified amount of 60 wt% PTFE emulsion (PTFE/CB = 0.3–1.5) was separately mixed with 4 mL deionized water and added dropwise to the CB dispersion during 1 h sonication. The resulting ink was spray-coated onto CP using a Catalyst Coating Membrane spray-coating device (CCM, HEPHAS Energy, China) under vacuum (substrate temperature: 60 °C; ink pressure: 0.25 MPa; atomization: 3.5 MPa; width: 1.0 MPa). Multiple layers were applied with 5 min intervals for drying. After spraying, electrodes were dried at 60 °C for 12 h. During the spray-coating and high-temperature drying steps, rapid solvent evaporation removed the surface-active agents in the PTFE emulsion. As these surfactants are soluble in the solvent phase, they volatilized together with the solvent. EDS analysis

of the as-prepared PPE electrodes (Supplementary Fig. 48) showed no oxygen signal from residual surfactants, confirming that the PTFE maintained its hydrophobicity without sintering.

Calcined particulate-packed electrode (PPE-cal): PPE electrodes were calcined at 340 °C for 1 h without hot pressing to induce partial PTFE melting while preserving the same macroscopic density as PPE.

Dual-layer porous/wettability electrode (PPE-D): The PPE-D electrode was prepared similarly to PPE, but with PTFE/CB ratios of 1.8–3.6. A dense base layer was first deposited (2 mL ink) and calcined at 340 °C for 1 h. A second layer was then spray-coated atop the first using the same method as PPE.

Three-layer wettability gradient electrode (PPE-T): PPE-D electrodes were subjected to oxygen plasma etching (100 W, 600 s) to create a top layer with enhanced hydrophilicity, yielding a triple-wettability CL.

For all electrodes, the catalyst mass was held constant, with PTFE content adjusted to control the binder/catalyst ratio. Electrode dimensions were 5 cm × 5 cm (total) and 3 cm × 3 cm (active area). The catalyst loading of the PPE and FSE electrodes was fixed at 6 mg cm<sup>-2</sup>, while PPE-D and PPE-T electrodes were prepared with a loading of 8 mg cm<sup>-2</sup>. The loading was controlled by the dispensed volume of catalyst ink during spray coating. The final mass loading was determined by weighing the coated electrode after drying, subtracting the mass of the pristine carbon paper, and dividing the net mass by the coated geometric area.

### Electrochemical H<sub>2</sub>O<sub>2</sub> production

Electrosynthesis of H<sub>2</sub>O<sub>2</sub> was conducted in a custom two-compartment cell (Supplementary Fig. 3) separated by a cation exchange membrane (CEM, Fumasep Fkb-pk-130), Na<sub>2</sub>SO<sub>4</sub> as the supporting electrolyte. Initially, the anode and cathode chambers contained 120 mL and 70 mL of electrolyte solution, respectively. The GDE (mass loading of 6 mg cm<sup>-2</sup>) cathode and a Ti/IrO<sub>2</sub>-Ta<sub>2</sub>O<sub>5</sub> anode (40 × 40 × 1 mm, Ir:Ta = 8:2, mass loading of 1 mg cm<sup>-2</sup>) were positioned 30 mm apart. The cathode GDL was exposed to ambient air without external aeration. Electrolysis was performed under magnetic stirring (500 rpm) and constant current conditions (15–400 mA cm<sup>-2</sup>), powered by a DC supply (0–20 A, 0–30 V). All measurements were conducted at room temperature (20 °C). At predetermined time intervals, 1 mL of catholyte was withdrawn using a micropipette for H<sub>2</sub>O<sub>2</sub> quantification. The remaining catholyte volume was measured simultaneously and used for Faradaic efficiency calculations.

Two testing modes were adopted. At low current densities (15, 100 mA cm<sup>-2</sup>), electrolysis was performed for 4 h in 0.1 mol L<sup>-1</sup> Na<sub>2</sub>SO<sub>4</sub> (pH = 5.84 ± 0.01), with H<sub>2</sub>O<sub>2</sub> concentrations sampled every 40 min. At high current densities (200–400 mA cm<sup>-2</sup>), 1 mol L<sup>-1</sup> Na<sub>2</sub>SO<sub>4</sub> (pH = 6.92 ± 0.06) was used, and periodic electrolyte replacement was employed to mitigate thermal decomposition. Each electrode was tested over five 1-h cycles, with H<sub>2</sub>O<sub>2</sub> yield and Faradaic efficiency calculated from collected samples. Error bars represent standard deviation from triplicate tests (*n* = 15).

Electrolysis under different pH conditions. To evaluate the generality of the structural design, electrochemical tests were conducted under acidic (1 mol L<sup>-1</sup> H<sub>2</sub>SO<sub>4</sub>, pH = 0.56 ± 0.03) and alkaline conditions (1 mol L<sup>-1</sup> NaOH, pH = 13.45 ± 0.02). The experiments were performed using the same self-breathing two-compartment cell (Supplementary Fig. 3) as described above. Constant-current electrolysis was carried out at a current density of 400 mA cm<sup>-2</sup>, and the hydrogen peroxide concentration after each cycle was determined by the potassium titanium oxalate method. Error bars represent standard deviation from tests (*n* = 3).

The floating gas diffusion electrode (GDE) performance under zero hydrostatic pressure was evaluated in a conventional single-compartment, membrane-free electrochemical cell (Supplementary Fig. 42) containing 300 mL of 1 mol L<sup>-1</sup> Na<sub>2</sub>SO<sub>4</sub> (pH = 6.92 ± 0.06). The

GDE was gently placed on the electrolyte surface to float freely without external pressure, and a platinum foil was used as the counter electrode. Chronoamperometric measurements were performed at a constant current density of 300 mA cm<sup>-2</sup>. PPE and PPE-T electrodes with mass loadings of 6 and 8 mg cm<sup>-2</sup>, respectively, were tested under identical conditions. After 30 min of electrolysis, the electrolyte was sampled for H<sub>2</sub>O<sub>2</sub> quantification to determine the Faradaic efficiency (FE). All measurements were conducted in triplicate (*n* = 3), and results are reported as mean values with standard deviations.

Commercial-scale self-breathing electrosynthesis experiments. Commercial-scale electrolysis experiments were carried out on a custom-built self-breathing electrosynthesis platform equipped with independent anodic and cathodic circulation systems, separated by a cation exchange membrane (Nafion 117, 110 × 110 mm × 183 μm). The electrolyzer operated under ambient pressure with natural air supply to the cathode side. The applied current density was 100 mA cm<sup>-2</sup>, and the system was operated in continuous circulation mode. The anolyte consisted of 5 mol L<sup>-1</sup> NaOH (pH = 14 ± 0.02) solution, which was periodically replenished with 32 wt% NaOH to maintain alkalinity. The catholyte was deionized water, recirculated in a closed loop. Temperature regulation was achieved through a built-in water-jacket heat exchanger integrated into both electrolyte tanks. A total of 1 L catholyte was used in each run and replaced every 2 h of recirculation. The system was operated for 10 h per day, followed by flushing with deionized water.

### GDE resistance pulse testing

**H<sub>2</sub>O<sub>2</sub> test strips preparation.** Qualitative filter paper was soaked in a solution of 5 mol L<sup>-1</sup> H<sub>2</sub>SO<sub>4</sub> and 0.1 mol L<sup>-1</sup> potassium titanium oxalate, then dried at 60 °C and cut to match the observation window size, yielding peroxide-sensitive test strips.

**Resistance pulse test.** An in situ breakthrough test was conducted to quantify the GDE's resistance to electrolyte intrusion. The GDE was mounted in a custom vertical setup in which 1 mol L<sup>-1</sup> Na<sub>2</sub>SO<sub>4</sub> was supplied through a scaled glass tube. The CL surface of the GDE was positioned at the 0 cm reference mark, and the hydrostatic pressure was controlled by adjusting the liquid height (*h*) above this level. A Pt electrode served as the counter electrode, while the GDE functioned as the cathode for H<sub>2</sub>O<sub>2</sub> generation under a constant applied voltage. During operation, the combined effects of hydrostatic pressure and electrowetting caused electrolyte to progressively intrude into the CL. Breakthrough was detected using a hydrogen peroxide indicator strip placed at the GDL side of the GDE; the appearance of a localized yellow discoloration marked the breakthrough point. The breakthrough time (*t*) corresponding to each preset liquid height (*h*) was recorded. The product of *h*·*t* was used to quantify flooding resistance.

The resistance impulse of the GDE is expressed as:

$$I = F \cdot t \quad (1)$$

$$F = \rho \cdot g \cdot h \cdot S \quad (2)$$

Where *I* is the resistance impulse of the GDE (N s). *F* is the force exerted on the GDE by the electrolyte pressure (N). *t* is the time (s). *ρ* is the density of the electrolyte (kg m<sup>-3</sup>). *g* is the gravitational acceleration (m s<sup>-2</sup>). *h* is the height of the electrolyte in the glass tube (m). *S* is the area of the GDE in contact with the electrolyte (m<sup>2</sup>).

### Electrode characterization

The morphology and elemental composition of the GDEs were characterized using field-emission scanning electron microscopy (FE-SEM, HITACHI SU8010) equipped with an energy-dispersive X-ray spectrometer (EDS, Oxford X-Max). Surface chemical states were analyzed by

X-ray photoelectron spectroscopy (XPS, PHI 5000 VersaProbe III). Static contact angles were measured using a goniometer (Krüss DSA25Basic).

Linear sweep voltammetry (LSV) curves were collected at a scan rate of  $20 \text{ mV s}^{-1}$  over a potential window of 0 to  $-4 \text{ V}$  vs. SCE in  $1 \text{ mol L}^{-1} \text{ Na}_2\text{SO}_4$  solution ( $\text{pH} = 6.92 \pm 0.06$ ), using a  $\text{Ti}/\text{IrO}_2\text{-Ta}_2\text{O}_5$  counter electrode. Electrochemical impedance spectroscopy (EIS) was conducted at open-circuit potential ( $-0.158 \text{ V}$ ) in the same electrolyte, with a frequency range of  $10^5$  to  $10^{-1} \text{ Hz}$  and an amplitude of  $5 \text{ mV}$ . EIS spectra were fitted using ZView software with an appropriate equivalent circuit.

Catalyst intrinsic activity and selectivity were evaluated using a rotating ring-disk electrode (RRDE, Pine Instruments) in  $\text{O}_2$ -saturated  $0.1 \text{ mol L}^{-1} \text{ KOH}$  ( $\text{pH} = 13 \pm 0.05$ ). Measurements were performed using a glassy carbon disk ( $0.2475 \text{ cm}^2$ ) and Pt ring ( $0.1866 \text{ cm}^2$ ,  $N = 0.37$ ) at  $1600 \text{ rpm}$  with a scan rate of  $10 \text{ mV s}^{-1}$ . Hydrophilic surface modification via plasma etching was performed using a CPC-Fplus plasma cleaner.

Stepwise chronoamperometry was conducted in  $1 \text{ mol L}^{-1} \text{ Na}_2\text{SO}_4$  solution ( $\text{pH} = 6.92 \pm 0.06$ ) to evaluate oxygen mass transfer under self-breathing conditions. The setup was identical to that used for  $\text{H}_2\text{O}_2$  electrosynthesis but operated in a three-electrode mode, with the GDE as the working electrode, SCE as the reference, and a  $\text{Ti}/\text{IrO}_2\text{-Ta}_2\text{O}_5$  mesh as the counter electrode. A current density of  $25 \text{ mA cm}^{-2}$  was applied initially, followed by  $25 \text{ mA cm}^{-2}$  increments every 3 min up to  $250 \text{ mA cm}^{-2}$ .  $\text{H}_2\text{O}_2$  concentrations were measured at the end of each step, and the net  $\text{H}_2\text{O}_2$  formed in each interval was used to calculate the Faradaic efficiency at steady state.

All electrochemical measurements were performed using a potentiostat/galvanostat (DongHua DH7000, China). All electrochemical potentials were measured against a saturated calomel electrode (SCE,  $+0.241 \text{ V}$  vs. NHE at  $25^\circ\text{C}$ , China). The reference electrode was calibrated prior to each set of experiments using a standard hydrogen electrode (SHE) in  $0.1 \text{ mol L}^{-1} \text{ H}_2\text{SO}_4$ . Potentials were converted to the reversible hydrogen electrode (RHE) scale using:

$$E_{\text{RHE}} = E_{\text{SCE}} + 0.242 + 0.059 \times \text{pH}$$

where  $0.242 \text{ V}$  is the standard potential of SCE versus NHE at  $25^\circ\text{C}$ . All potentials reported in this work are presented without  $iR$  compensation unless otherwise stated. The solution resistance ( $R_s$ ) was measured by high-frequency EIS for each electrolyte, with typical values of  $4.55 \pm 0.6 \Omega$  in  $1 \text{ mol L}^{-1} \text{ Na}_2\text{SO}_4$  (LSV measurements) and  $37.7 \pm 0.6 \Omega$  in  $0.1 \text{ mol L}^{-1} \text{ KOH}$  (RRDE measurements).

Pore structure parameters including size distribution, permeability, and tortuosity were obtained by mercury intrusion porosimetry (Micromeritics AutoPore IV 9500,  $0.5\text{--}33,000 \text{ psi}$ ). 3D CL morphology was reconstructed using FIB-SEM (FEI Helios Nanolab G3 UC). Catalyst ink particle size distribution was measured with a laser diffraction analyzer (Bettersize2600).

### **$\text{H}_2\text{O}_2$ product quantification**

The concentration of the produced  $\text{H}_2\text{O}_2$  was determined using a UV-Vis spectrophotometer (Agilent Technologies, Inc., USA) and the potassium titanium (IV) oxalate method at  $\lambda = 400 \text{ nm}$ <sup>14</sup>. Potassium titanium (IV) oxalate can react with  $\text{H}_2\text{O}_2$  to form a stable yellow-orange titanium (IV)-peroxide complex, with its color depth being proportional to the  $\text{H}_2\text{O}_2$  concentration. Different dilution factors were chosen based on the current density, and samples were diluted before measurement. The standard curve for  $\text{H}_2\text{O}_2$  quantification was shown in Supplementary Fig. 49. No additional liquid- or gas-phase products were detected. This is consistent with the inert  $\text{Na}_2\text{SO}_4$  electrolyte, where dissolved  $\text{O}_2$  is the only reducible species. Faradaic efficiency

(FE) was calculated using the following formula, based on the measured concentration and the volume of electrolyte in the cathode compartment at each sampling time:

$$\text{FE}(\%) = \frac{nFCV}{It} \times 100\% \quad (3)$$

where  $n$  is the number of electrons transferred for  $\text{O}_2$  reduction to  $\text{H}_2\text{O}_2$  ( $n = 2$ ),  $F$  is the Faraday constant ( $96486 \text{ C mol}^{-1}$ ),  $C$  is the concentration of  $\text{H}_2\text{O}_2$  ( $\text{mol L}^{-1}$ ),  $V$  is the volume of electrolyte (L),  $I$  is the current (A), and  $t$  is the electrolysis time (s). All FE values reported in this study were obtained under galvanostatic operation at the specified current densities.

### **PTFE-based ink preparation/dispersion optimization**

Nine PTFE-containing mixed solutions were prepared using various sequences, solvent compositions, and ultrasonication conditions. Each formulation consisted of  $4 \text{ mL}$  (or  $2 \text{ mL}$ ) deionized water,  $5 \text{ mL}$  isopropanol, and  $0.15 \text{ mL}$  of  $5 \text{ wt}\%$  PTFE emulsion. The mixtures were ultrasonicated at either  $10^\circ\text{C}$  or  $40^\circ\text{C}$ . Nine different mixing methods were as follows (Supplementary Fig. 11):

1. PTFE emulsion was directly added to isopropanol, followed by water. Ultrasonication was performed at  $10^\circ\text{C}$ .
2. PTFE emulsion was first diluted with water, then added all at once to isopropanol. Ultrasonication was performed at  $10^\circ\text{C}$ .
3. PTFE emulsion was first diluted with water, then slowly added dropwise into isopropanol. Ultrasonication was performed at  $10^\circ\text{C}$ .
4. PTFE emulsion was directly added to isopropanol, followed by water. Ultrasonication was performed at  $40^\circ\text{C}$ .
5. PTFE emulsion was first diluted with water, then added all at once to isopropanol. Ultrasonication was performed at  $40^\circ\text{C}$ .
6. PTFE emulsion was first diluted with water, then slowly added dropwise into isopropanol. Ultrasonication was performed at  $40^\circ\text{C}$ .
7. Using  $2 \text{ mL}$  water instead of  $4 \text{ mL}$ , PTFE emulsion was directly added to isopropanol, followed by water. Ultrasonication was performed at  $40^\circ\text{C}$ .
8. Using  $2 \text{ mL}$  water, PTFE emulsion was first diluted with water, then added all at once to isopropanol. Ultrasonication was performed at  $40^\circ\text{C}$ .
9. Using  $2 \text{ mL}$  water, PTFE emulsion was first diluted with water, then slowly added dropwise into isopropanol. Ultrasonication was performed at  $40^\circ\text{C}$ .

### **FIB-SEM 3D reconstruction method**

Electrodes were cut into  $5 \text{ mm} \times 5 \text{ mm}$  pieces, washed with ethanol, and vacuum-impregnated with epoxy resin for  $12 \text{ h}$  before curing at  $65^\circ\text{C}$ . After hardening, samples were mounted in the FIB-SEM (FEI Helios Nanolab G3 UC) and sequentially imaged at  $5 \text{ nm}$  slicing intervals, yielding  $600$  images ( $3 \times 2.5 \mu\text{m}^2$ ). Two sample-preparation approaches were evaluated prior to FIB-SEM imaging: (i) epoxy embedding, which provided mechanical stability and was therefore used for all analyses presented in the main text, and (ii) direct cutting and loading of unembedded electrodes, which was examined only for comparison. A detailed discussion of the differences between these approaches is provided in Supplementary Note 1.

3D reconstruction was performed using Avizo. Image stacks were auto-aligned, and noise and curtaining artifacts were removed using FFT filtering, mean filtering, non-local means (NLM), and anisotropic diffusion. Solid and pore phases were segmented using Otsu's thresholding, followed by gray-level-based segmentation to distinguish carbon black (CB) and PTFE. Boolean operations were then used

to isolate CB and pore domains, and voxel interpolation was applied to generate the final 3D structure (Fig. S12).

### Quartet structure generation set method

The 3D catalyst layer (CL) structure was generated using the Quartet Structure Generation Set (QSGS) method proposed by Wang et al.<sup>54</sup>. This stochastic algorithm controls phase morphology via four parameters: nucleation probability ( $P_c$ ), directional growth probability ( $P_i$ ), inter-phase attachment probability ( $P_i^{nm}$ ), and target phase volume fraction ( $R_p$ ).  $P_c$  determines the initial spatial distribution of nucleation sites; lower values promote localized aggregation.  $P_i$  governs anisotropic phase growth along 26 discrete directions (cube vertices, edges, and faces), with direction-specific probabilities listed in Supplementary Table 4. Given the anisotropic, particulate morphology observed in FIB-SEM images, PTFE and CB phases were modeled with non-uniform  $P_i$  values.  $P_i^{nm}$  defines the interaction between phases, such as CB attachment to PTFE. Growth proceeds iteratively until each phase reaches the predefined volume fraction  $R_p$ .

Three-dimensional CL structures of the FSE and PPE electrodes were reconstructed using the QSGS method (Fig. S7). In addition to these, five representative QSGS-generated structures were produced to systematically examine the effects of PTFE loading and dispersion (Fig. S21). Structures (1), (2), and (3) share the same PTFE nucleation probability ( $P_c$ ) but exhibit increasing PTFE volume fractions ( $R_p$ ), mimicking CLs prepared from inks with identical dispersion conditions but different PTFE loadings. Structures (2), (4), and (5) maintain a constant  $R_p$  while varying  $P_c$ , corresponding to identical ink compositions subjected to different dispersion qualities. Increasing  $P_c$  results in more uniform PTFE/CB mixing with fewer aggregated PTFE domains. In addition, multiple QSGS reconstructions were performed to obtain the three-dimensional structure of the gradient-engineered PPE-T catalyst layer.

### Lattice Boltzmann method

To accurately simulate two-phase flow within the CL, we used the phase-field lattice Boltzmann equation developed by Long et al., which is capable of predicting the wetting behavior of fluid pairs with large density ratios. In this model, the liquid-solid free energy is treated as part of the chemical potential rather than as a boundary condition, simplifying the implementation of wetting boundary conditions. Additionally, the AC equation is solved using a well-balanced LBE model, which further improves numerical stability and ensures accurate prediction of two-phase flow and wetting behavior with large density ratios. The LBM program was implemented in C++ and parallelized using the CUDA platform and GPU for efficient computation<sup>45,46</sup>.

The conservative Allen–Cahn equation can be expressed by

$$\frac{\partial \phi}{\partial t} + \nabla \cdot (\phi \mathbf{u}) = \nabla \cdot [M(\nabla \phi - \lambda \mathbf{n})] \quad (4)$$

where  $M$  is the mobility,  $\mathbf{n}$  is the unit vector normal to the interface.  $\lambda$  is a function of  $\phi$ .  $\phi$  taking 1 and 0 represents the liquid and gas phase fluids. The fluid velocity  $\mathbf{u}$  in Eq.(S2) is governed by the following Navier–Stokes equations with the force,

$$\nabla \cdot \mathbf{u} = \mathbf{0} \quad (5)$$

$$\frac{\partial (\rho \mathbf{u})}{\partial t} + \nabla \cdot (\rho \mathbf{u} \mathbf{u}) = -\nabla p + \nabla \cdot [\mu(\nabla \mathbf{u} - \nabla \mathbf{u}^T)] + F_S + G \quad (6)$$

where  $\rho$  is the fluid density,  $p$  is the hydrodynamic pressure,  $\mu$  is the dynamic viscosity by  $\mu = \rho \nu$ ,  $\nu$  is the kinematic viscosity,  $F_S$  is the surface tension force, and  $G$  is the possible body force.

The LB evolution equation with the BGK collision operator for the conservative Allen–Cahn equation can be written as

$$f_i(\mathbf{x} + \mathbf{c}_i \delta_t, t + \delta_t) - f_i(\mathbf{x}, t) = -\frac{1}{\tau_f} [f_i(\mathbf{x}, t) - f_i^{eq}(\mathbf{x}, t)] + \delta_t F_i(\mathbf{x}, t) \quad (7)$$

$$f_i^{eq} = \omega_i \phi \left( 1 + \frac{\mathbf{c}_i \cdot \mathbf{u}}{c_s^2} \right) \quad (8)$$

where  $f_i(\mathbf{x}, t)$  is the particle distribution function,  $\tau_f$  is the nondimensional relaxation time related to the mobility,  $F_i(\mathbf{x}, t)$  is the source term, and a simple form of the  $f_i^{eq}(\mathbf{x}, t)$  is equilibrium distribution function,  $c_s$  is the sound speed,  $\mathbf{c}_i$  are the discrete velocities, and  $\omega_i$  are the weighting coefficients.

The order parameter in the present model can be computed by

$$\phi = \sum_i f_i \quad (9)$$

The distribution of fluid density in a two-phase system physically is consistent with that of the order parameter. To satisfy this physical property, the fluid density should take the linear interpolation,

$$\rho = \phi(\rho_l - \rho_g) + \rho_g \quad (10)$$

where  $\rho_l$  and  $\rho_g$  represent the densities of the liquid and gas phases.

This version clarifies that additional details regarding wetting boundary optimization can be found in the cited references.

**Electrolyte invasion model.** Electrolyte intrusion into the catalyst layer was simulated using a multiphase lattice Boltzmann model. The liquid phase was injected from one side of the catalyst layer with a constant inlet velocity, while the opposite side was defined as an outlet boundary condition with non-gradient constraints for pressure and velocity. The remaining four faces of the domain were treated as periodic boundaries to mimic an infinitely extended porous medium. The physical size of the simulated subvolume was  $2 \times 2 \times 3 \mu\text{m}^3$ , consistent with the FIB-SEM reconstructed catalyst layer used in Fig. S18.

**Self-transport of in situ generated  $\text{H}_2\text{O}_2$ .** To mimic the in situ electrogeneration and subsequent transport of  $\text{H}_2\text{O}_2$  inside the catalyst layer, a second lattice Boltzmann model was constructed in which a local water source term was imposed at the center of the reconstructed catalyst layer domain to represent  $\text{H}_2\text{O}_2$  formation at active sites. Both through-plane ends of the catalyst layer were specified as outlet boundaries with non-gradient conditions for velocity and scalar fields, allowing the generated  $\text{H}_2\text{O}_2$  solution to leave the domain from either side. The remaining four faces were defined as constant-velocity inlet boundaries to maintain a steady convective flow of electrolyte through the porous structure. The detailed boundary configuration for this model is shown in Fig. S43.

### Saturation

The saturation of each phase is calculated as follows:

$$S_L = \frac{\varepsilon_L}{\varepsilon} S_A = \frac{\varepsilon_A}{\varepsilon} \quad (11)$$

where  $\varepsilon_L$  and  $\varepsilon_A$  are the porosity of liquid and air, which denote the amount of space occupied by the liquid and air, respectively. Therefore, saturation is defined as the ratio of each phase to the porosity of the porous media<sup>55</sup>.

## Molecular dynamics

Atomistic molecular dynamics simulations have been performed in the GROMACS<sup>56</sup> (version 2022.6) simulation package using the CHARMM 36 force field<sup>57</sup> and the water molecules were modeled using the TIP3P water model. PTFE molecules were first placed on both sides of a slice of C<sub>54</sub> carbon sheets filled with 300 H<sub>2</sub>O<sub>2</sub> molecules. The first system has 40 chains on top and 10 on the bottom, and the other system has 25 chains on both sides. For both systems, the upper layer was filled with 500 O<sub>2</sub> molecules and 2000 water molecules, the lower layer was filled with around 4000 water molecules, resulting in a system size of 5 × 5 × 12 nm. On both side of the simulation box, implicit walls were placed to prevent molecules moving to the other side through the periodic boundary. After thousands of steps of energy minimization, the system was equilibrated for 500 ps followed by 4000 ps production molecular dynamics process under the canonic ensemble. An integration time-step of 1 fs was used and the temperature was coupled to 298 K using the Nose-Hoover method and a cutoff scheme of 1.2 nm was used for the non-bonded interactions, and the Particle Mesh Ewald method<sup>58</sup> with a fourierspacing of 0.1 nm was applied for the long range electrostatic interactions. All covalent bonds with hydrogen atoms were constraint using the LINCS algorithm<sup>59</sup>. The mean squared displacements (MSD) of O<sub>2</sub> and H<sub>2</sub>O<sub>2</sub> molecules in different systems were calculated to quantify their mass-transfer behavior. The MSD is calculated as follows:

$$\text{MSD} = \frac{1}{N} \sum_{i=1}^N |\Delta \vec{r}_i(t)|^2 \quad (12)$$

## Data availability

Source data for all graphs presented in the main manuscript and the Supplementary Information are available via figshare at <https://doi.org/10.6084/m9.figshare.29529032> and are also provided in the accompanying Source Data file. Simulation files, QSGS-reconstructed structures, physical-model input files, and analysis codes have been deposited in Zenodo under accession code <https://doi.org/10.5281/zenodo.17909038>. Source data are provided with this paper.

## Code availability

All codes used in this study—including the LBM solver, QSGS reconstruction scripts, and the analysis scripts—have been deposited in the Zenodo repository under accession code <https://doi.org/10.5281/zenodo.17788649>. All codes are openly accessible without restriction.

## References

- Lewis, R. J. et al. Highly efficient catalytic production of oximes from ketones using in situ-generated H<sub>2</sub>O<sub>2</sub>. *Science* **376**, 615 (2022).
- Deng, Z. P., Choi, S. J., Li, G. & Wang, X. L. Advancing H<sub>2</sub>O<sub>2</sub> electrosynthesis: enhancing electrochemical systems, unveiling emerging applications, and seizing opportunities. *Chem. Soc. Rev.* **53**, 8137–8181 (2024).
- Xia, C., Xia, Y., Zhu, P., Fan, L. & Wang, H. Direct electrosynthesis of pure aqueous H<sub>2</sub>O<sub>2</sub> solutions up to 20% by weight using a solid electrolyte. *Science* **366**, 226 (2019).
- Yu, A., Liu, S. W. & Yang, Y. Recent advances in electrosynthesis of H<sub>2</sub>O<sub>2</sub> via two-electron oxygen reduction reaction. *Chem. Commun.* **60**, 5232–5244 (2024).
- Holade, Y., Ghosh, S. & Napporn, T. W. Best practices for hydrogen peroxide (photo)electrosynthesis. *Nat. Sustain.* **7**, 1085–1087 (2024).
- Zheng, Y. S. et al. Boosting hydrogen peroxide accumulation by a novel air-breathing gas diffusion electrode in electro-Fenton system. *Appl. Catal. B Environ.* **316**, 121617 (2022).
- Xu, J. W. et al. Organic wastewater treatment by a single-atom catalyst and electrolytically produced H<sub>2</sub>O<sub>2</sub>. *Nat. Sustain.* **4**, 233–241 (2021).
- Gu, Y. et al. Industrial electrosynthesis of hydrogen peroxide over *p*-block metal single sites. *Nat. Synth.* **4**, 614–621 (2025).
- Yu, Z. Y. et al. Selective and durable H<sub>2</sub>O<sub>2</sub> electrosynthesis catalyst in acid by selenization induced straining and phasing. *Nat. Commun.* **15**, 9346 (2024).
- An, J. K. et al. Amplifying anti-flooding electrode to fabricate modular electro-fenton system for degradation of antiviral drug lamivudine in wastewater. *J. Hazard. Mater.* **428**, 128185 (2022).
- Zhao, Q. et al. Superhydrophobic air-breathing cathode for efficient hydrogen peroxide generation through two-electron pathway oxygen reduction reaction. *ACS Appl. Mater. Inter.* **11**, 35410–35419 (2019).
- Zhang, Q. Z. et al. Highly efficient electrosynthesis of hydrogen peroxide on a superhydrophobic three-phase interface by natural air diffusion. *Nat. Commun.* **11**, 1731 (2020).
- Li, H. H., Quispe-Cardenas, E., Yang, S. S., Yin, L. F. & Yang, Y. Electrosynthesis of >20 g/L H<sub>2</sub>O<sub>2</sub> from Air. *Acs Est. Eng.* **2**, 242–250 (2022).
- Cui, L. L. et al. An anti-electrowetting carbon film electrode with self-sustained aeration for industrial H<sub>2</sub>O<sub>2</sub> electrosynthesis. *Energy Environ. Sci.* **17**, 655–667 (2024).
- An, J. K. et al. Highly efficient electro-generation of H<sub>2</sub>O<sub>2</sub> by adjusting liquid-gas solid three phase interfaces of porous carbonaceous cathode during oxygen reduction reaction. *Water Res.* **164**, 114933 (2019).
- Wang, S. L. et al. Beyond the catalyst: a robust and omnidirectional hydrophobic triple-phase architecture for ameliorating air-breathing H<sub>2</sub>O<sub>2</sub> electrosynthesis and wastewater remediation. *Sep. Purif. Technol.* **305**, 122397 (2023).
- Yu, S. C. et al. Preparation of microporous layer for proton exchange membrane fuel cell by using polyvinylpyrrolidone aqueous solution. *Int. J. Hydrog. Energy* **39**, 15681–15686 (2014).
- Pan, W. T. et al. Microstructure and macroscopic rheology of microporous layer nanoinks for PEM fuel cells. *Chem. Eng. Sci.* **246**, 117001 (2021).
- Ding, P. P., Cui, L. L., Li, D. & Jing, W. H. Innovative dual-compartment flow reactor coupled with a gas diffusion electrode for in situ generation of H<sub>2</sub>O<sub>2</sub>. *Ind. Eng. Chem. Res.* **58**, 6925–6932 (2019).
- Tian, Q. et al. Hydrogen peroxide electrosynthesis via selective oxygen reduction reactions through interfacial reaction micro-environment engineering. *Adv. Mater.* **37**, 2414490 (2025).
- Li, Q. et al. Effect of porous transport layer wettability on oxygen transportation in proton exchange membrane water electrolysis. *J. Power Sources* **606**, 234554 (2024).
- Wang, S. L. et al. Engineering a concordant microenvironment with air-liquid-solid interface to promote electrochemical H<sub>2</sub>O<sub>2</sub> generation and wastewater purification. *Sep. Purif. Technol.* **297**, 121527 (2022).
- Cui, L. L. et al. Species mass transfer governs the selectivity of gas diffusion electrodes toward H<sub>2</sub>O<sub>2</sub> electrosynthesis. *Nat. Commun.* **15**, 10632 (2024).
- Sun, Y. et al. Rational design of an air-breathing gas-diffusion electrode with oxygen vacancy-rich ZnO for robust and durable H<sub>2</sub>O<sub>2</sub> electrosynthesis. *Chem. Eng. J.* **500**, 157563 (2024).
- Li, L. et al. Direct hydrogen peroxide synthesis on a Sn-doped CuWO<sub>4</sub>/Sn anode and an air-breathing cathode. *Chem. Mater.* **34**, 63–71 (2022).
- Shen, C. et al. A numerical simulation study on the spontaneous imbibition and hydro-thermal coupling in soil using the lattice Boltzmann method. *Int. Commun. Heat Mass Transf.* **159**, 108048 (2024).

27. Wang, Z. Y., Jin, X., Wang, X. Q., Sun, L. & Wang, M. R. Pore-scale geometry effects on gas permeability in shale. *J. Nat. Gas Sci. Eng.* **34**, 948–957 (2016).
28. Li, Q., Du, D. H., Fei, L. L. & Luo, K. H. Three-dimensional non-orthogonal MRT pseudopotential lattice Boltzmann model for multiphase flows. *Comput. Fluids* **186**, 128–140 (2019).
29. Wang, Y. D. et al. Large-scale physically accurate modelling of real proton exchange membrane fuel cell with deep learning. *Nat. Commun.* **14**, 745 (2023).
30. Chen, F. D. et al. Overcoming the limitation of ionomers on mass transport and Pt activity to achieve high-performing membrane electrode assembly. *J. Am. Chem. Soc.* **146**, 30388–30396 (2024).
31. Sui, W. B. et al. Efficient and durable electrochemical oxygen reduction to H<sub>2</sub>O<sub>2</sub> in acidic media assisted through catalyst layer design. *J. Power Sources* **556**, 232438 (2023).
32. Zhao, E. R. et al. Technoeconomic assessment of electrochemical hydrogen peroxide production with gas diffusion electrodes under scenarios relevant to practical water treatment. *ACS Est. Eng.* **3**, 1800–1812 (2023).
33. Lin, Z. H. et al. Atomic Co decorated free-standing graphene electrode assembly for efficient hydrogen peroxide production in acid. *Energ. Environ. Sci.* **15**, 1172–1182 (2022).
34. Wang, J. W., Li, C. L., Rauf, M. & Wang, W. H. Highly efficient H<sub>2</sub>O<sub>2</sub> electrogeneration enabled by controlling the wettability of gas diffusion electrodes and the reaction pathway in divided cells. *ACS Sustain. Chem. Eng.* **11**, 436–443 (2023).
35. Li, B. et al. Controlling the microscopic morphology and permeability of catalyst layers in proton exchange membrane fuel cells by adjusting catalyst ink agglomerates. *Int. J. Hydrog. Energy* **46**, 32215–32225 (2021).
36. Lei, C. et al. Impact of catalyst ink dispersing solvent on PEM fuel cell performance and durability. *J. Electrochem. Soc.* **168**, 044517 (2021).
37. Sim, J., Kang, M. & Min, K. Effects of basic gas diffusion layer components on PEMFC performance with capillary pressure gradient. *Int. J. Hydrog. Energy* **46**, 27731–27748 (2021).
38. Stampino, P. G. et al. Effect of different substrates, inks composition and rheology on coating deposition of microporous layer (MPL) for PEM-FCs. *Catal. Today* **147**, S30–S35 (2009).
39. Ngo, T. T., Yu, T. L. & Lin, H. L. Influence of the composition of isopropyl alcohol/water mixture solvents in catalyst ink solutions on proton exchange membrane fuel cell performance. *J. Power Sources* **225**, 293–303 (2013).
40. Ma, S., Chen, Q., Jogensen, F. H., Stein, P. C. & Skou, E. M. <sup>19</sup>F NMR studies of Nafion™ ionomer adsorption on PEMFC catalysts and supporting carbons. *Solid State Ion.* **178**, 1568–1575 (2007).
41. Qian, G. Y. et al. Revealing the aging process of solid electrolyte interphase on SiO<sub>x</sub> anode. *Nat. Commun.* **14**, 6048 (2023).
42. O'Brien, C. P. et al. Scalability and stability in CO<sub>2</sub> reduction via tomography-guided system design. *Joule* **8**, 2903–2919 (2024).
43. Inoue, G. et al. Theoretical examination of effective oxygen diffusion coefficient and electrical conductivity of polymer electrolyte fuel cell porous components. *J. Power Sources* **327**, 610–621 (2016).
44. Bachmann, M. D. et al. Directional ballistic transport in the two-dimensional metal PdCoO<sub>2</sub>. *Nat. Phys.* **18**, 819 (2022).
45. Ju, L., Guo, Z. L., Yan, B. C. & Sun, S. Y. Implementation of contact line motion based on the phase-field lattice Boltzmann method. *Phys. Rev. E* **109**, 045307 (2024).
46. Ju, L., Shan, B. C., Yang, Z. & Guo, Z. L. An exact non-equilibrium extrapolation scheme for pressure and velocity boundary conditions with large gradients in the lattice Boltzmann method. *Comput. Fluids* **231**, 105163 (2021).
47. Guo, L. Y., Chen, L., Zhang, R. Y., Peng, M. & Tao, W. Q. Pore-scale simulation of two-phase flow and oxygen reactive transport in gas diffusion layer of proton exchange membrane fuel cells: effects of nonuniform wettability and porosity. *Energy* **253**, 124101 (2022).
48. Yu, J. L., Froning, D., Reimer, U. & Lehnert, W. Polytetrafluoroethylene effects on liquid water flowing through the gas diffusion layer of polymer electrolyte membrane fuel cells. *J. Power Sources* **438**, 226975 (2019).
49. Ruggiero, B. N. et al. Local reaction microenvironment impacts on H<sub>2</sub>O<sub>2</sub> electrosynthesis in a dual membrane electrode assembly solid electrolyte electrolyzer. *Chem. Eng. J.* **486**, 150246 (2024).
50. Ling, C. et al. Promoting the electrochemical water oxidation reaction to H<sub>2</sub>O<sub>2</sub> via bubbles on the electrode. *ACS Sustain. Chem. Eng.* **11**, 10264–10273 (2023).
51. de Anna, P., Pahlavan, A. A., Yawata, Y., Stocker, R. & Juanes, R. Chemotaxis under flow disorder shapes microbial dispersion in porous media. *Nat. Phys.* **17**, 68–73 (2021).
52. Zhao, E. et al. Optimization and scaling-up of porous solid electrolyte electrochemical reactors for hydrogen peroxide electrosynthesis. *Nat. Commun.* **16**, 3212 (2025).
53. Cao, P. K. et al. Durable and selective electrochemical H<sub>2</sub>O<sub>2</sub> synthesis under a large current enabled by the cathode with highly hydrophobic three-phase architecture. *ACS Catal.* **11**, 13797–13808 (2021).
54. Wang, M. & Pan, N. Numerical analyses of effective dielectric constant of multiphase microporous media. *J. Appl. Phys.* **101**, 8 (2007).
55. Cho, J. Y., Lee, H. M., Kim, J. H., Lee, W. & Lee, J. S. Numerical simulation of gas-liquid transport in porous media using 3D color-gradient lattice Boltzmann method: trapped air and oxygen diffusion coefficient analysis. *Eng. Appl. Comp. Fluid Mech.* **16**, 177–195 (2022).
56. Hess, B., Kutzner, C., David, V. D. S. & Lindahl, E. GROMACS 4: algorithms for highly efficient, load-balanced, and scalable molecular simulation. *J. Chem. Theory Comput.* **4**, 435–447 (2008).
57. Best, R. B., Zhu, X., Shim, J., Lopes, P. E. M. & Mackerell, A. D. Optimization of the additive CHARMM all-atom protein force field targeting improved sampling of the backbone  $\phi$ ,  $\psi$  and side-chain  $\chi(1)$  and  $\chi(2)$  dihedral angles. *J. Chem. Theory Comput.* **8**, 3257–3273 (2012).
58. Essmann, U. et al. A smooth particle mesh Ewald method. *J. Chem. Phys.* **103**, 8577–8593 (1995).
59. Hess, B., Bekker, H., Berendsen, H. J. C. & Fraaije, J. G. E. M. LINCS: a linear constraint solver for molecular simulations. *J. Comput. Chem.* **18**, 1463–1472 (1997).

## Acknowledgements

This research was supported by the National Key Research and Development Program of China (2022YFD2001705; Z.Y.), National Modern Agriculture Industrial Technology System (No. CARS-45-24; Z.Y.), Zhejiang University—Yuhang Joint Research Center for Smart Fisheries (2025SAKFJJ08; Z.Y.) and National Natural Science Foundation of China (No. 32303071; S.W.).

## Author contributions

Y.T., Z.Z., and Z.Y. conceived and designed the project. Y.T. and L.P. fabricated the electrodes and conducted performance evaluations. Y.T., S.W., and K.Y. designed and developed the pilot-scale electrolyzer system with assistance from S.Z. and Y.L. X.Y. performed the electrochemical characterization of the electrodes. Theoretical simulations, including LBM and MD modeling, were carried out by Y.T. and Y.X. under the guidance of Z.Z. and Z.Y. L.P., Y.L., and Z.Y. contributed to the development of the commercial-scale integrated platform. Data analysis and manuscript drafting were performed by Y.T. and S.W. The manuscript was revised and finalized by Z.Z. and Z.Y.

## Competing interests

The authors declare no competing interests.

## Additional information

**Supplementary information** The online version contains supplementary material available at <https://doi.org/10.1038/s41467-026-68436-x>.

**Correspondence** and requests for materials should be addressed to Zhenghua Zhang or Zhangying Ye.

**Peer review information** *Nature Communications* thanks Fengxia Deng and the other anonymous reviewer(s) for their contribution to the peer review of this work. A peer review file is available.

**Reprints and permissions information** is available at <http://www.nature.com/reprints>

**Publisher's note** Springer Nature remains neutral with regard to jurisdictional claims in published maps and institutional affiliations.

**Open Access** This article is licensed under a Creative Commons Attribution-NonCommercial-NoDerivatives 4.0 International License, which permits any non-commercial use, sharing, distribution and reproduction in any medium or format, as long as you give appropriate credit to the original author(s) and the source, provide a link to the Creative Commons licence, and indicate if you modified the licensed material. You do not have permission under this licence to share adapted material derived from this article or parts of it. The images or other third party material in this article are included in the article's Creative Commons licence, unless indicated otherwise in a credit line to the material. If material is not included in the article's Creative Commons licence and your intended use is not permitted by statutory regulation or exceeds the permitted use, you will need to obtain permission directly from the copyright holder. To view a copy of this licence, visit <http://creativecommons.org/licenses/by-nc-nd/4.0/>.

© The Author(s) 2026